

The OscSNS White Paper

October 9, 2018

M. Elnimr, I. Stancu

University of Alabama, Tuscaloosa, AL 35487

M. Yeh

Brookhaven National Laboratory, Upton, NY 11973

R. Svoboda

University of California, Davis, CA 95616

M. J. Wetstein

University of Chicago, Chicago, IL 60637

F. G. Garcia

Fermi National Accelerator Laboratory, Batavia, IL 60510

B. Osmanov, H. Ray

University of Florida, Gainesville, FL 32611

R. Tayloe

Indiana University, Bloomington, IN 47405

J. Boissevain, G. T. Garvey, W. Huelsnitz, W. C. Louis, G. B. Mills,

Z. Pavlovic, R. Van de Water, D. H. White

Los Alamos National Laboratory, Los Alamos, NM 87545

R. Imlay

Louisiana State University, Baton Rouge, LA 70803

B. P. Roe

University of Michigan, Ann Arbor, MI 48109

R. Allen

Oak Ridge National Laboratory, Oak Ridge, TN 37831

Y. Efremenko, T. Gabriel, T. Handler, Y. Kamyshkov

University of Tennessee, Knoxville, TN 37996

F. T. Avignone, S. R. Mishra, C. Rosenfeld

University of South Carolina, Columbia, SC 29208

J. M. Link

Virginia Tech, Blacksburg, VA 24060

Contact Persons: H. Ray and W. C. Louis

Contents

1	Executive Summary	9
2	Physics Goals	11
3	Path to Funding	17
3.1	Why the SNS?	17
3.1.1	SNS vs FNAL facilities	17
3.1.2	SNS vs All Other World Facilities	18
3.2	Why OscSNS is Unique	18
3.2.1	Complementariness to Other Experiments	19
3.2.2	DOE Mission Need	19
3.3	Path to Funding	19
4	The SNS Neutrino Source	21
4.1	The Accelerator and the Target Station	22
5	The OscSNS Detector	28
5.1	Overview	28
5.2	Rectangular Vault	35
5.3	Cylindrical Tank	35
5.4	Cylindrical Tank Internals	35
5.5	Detector Enclosure	36

5.6	Gadolinium-loaded Liquid Scintillator Option	36
5.7	Electronics and Data Acquisition	38
5.8	Calibration	38
6	SNS Neutrino Flux Simulation	40
6.1	Generation of Neutrino Fluxes	41
6.1.1	Generation of Primary Particles	41
6.1.2	Description of Geometry	41
6.1.3	Description of Physics Processes	41
6.1.4	Particle Counters and Histograms.	43
6.2	Simulation of Neutrino Interactions	47
7	OscSNS Detector Simulation	48
8	Event Reconstruction and Particle Identification	50
9	Event Rates and Sensitivity Predictions	53
9.1	Cross Section and Target Information	53
9.2	Total Expected Flux	56
9.3	Disappearance Sensitivity	57
9.4	Appearance Sensitivity : $\bar{\nu}_\mu \rightarrow \bar{\nu}_e, \nu_\mu \rightarrow \nu_e$	57
9.5	Event Rates and Background Estimates	58
9.5.1	ν_μ Disappearance Analysis	58
9.5.2	ν_e Disappearance Analysis	60
9.5.3	$\bar{\nu}_\mu \rightarrow \bar{\nu}_e$ Appearance Analysis	60
9.5.4	$\nu_\mu \rightarrow \nu_e$ Appearance Analysis	62
9.5.5	Oscillation Analysis Summary	63
9.5.6	Cross Section Analyses	64
10	L/E Distributions	66
11	Cost & Schedule	74

12 The OscSNS Near Detector	75
12.0.7 The OscSNS Near Detector	75
13 Appendix A - Letters of Support	76
14 Appendix B - BWSC Cost Estimate	77

List of Tables

2.1	Summary of per calendar year event rate predictions for a detector located at the SNS, centered at a distance of 60 meters from the interaction point, at ~ 150 degrees in the backward direction from the proton beam. The first column is the oscillation channel, the second column is the expected intrinsic background, and the third column is the expected signal for appearance searches and the total number of events for disappearance searches. All event rates account for a 50% detector efficiency, a 50% beam-on efficiency, a fiducial volume of 523 m^3 , and are in units of expected events per calendar year. Appearance signal estimates assume a 0.26% oscillation probability.	13
4.1	SNS design parameters.	25
6.1	Lifetime values for negative muons calculated with Geant4, compared to experimental data. Data is taken from [17]	43
7.1	Scintillation time constants, and relative yields of fast and slow scintillation light used in simulation. Values are taken from [20], see text for details.	49
9.1	Summary of per calendar year event rate predictions for a detector located at the SNS a distance of 60 meters from the interaction point, at ~ 150 degrees in the backward direction from the proton beam. The first column is oscillation channel, the second column is the expected intrinsic background, and the third column is the expected signal for appearance searches and the total number of events for disappearance searches. All event rates account for a 50% detector efficiency, a 50% beam-on efficiency, and a fiducial volume of 523 m^3 , and are in units of expected events per calendar year. Appearance signal estimates assume a 0.26% oscillation probability.	64
9.2	Summary of per calendar year event rate predictions for a detector located at the SNS a distance of 60 meters from the neutrino source, at ~ 150 degrees in the backward direction from the proton beam. The first column is cross section channel, the second column is the expected event rate. All event rates account for a 50% detector efficiency and a 50% beam-on efficiency, and are in units of expected events per year.	65

10.1	The average shape-only χ^2 values (for 10 data bins assuming no oscillations) after 10 calendar years of data taking for $\bar{\nu}_e$ appearance, ν_e disappearance, and ν_μ disappearance, taking into account the expected backgrounds. Also shown are the corresponding probabilities for no oscillations.	67
10.2	The average normalized χ^2 values (for 10 data bins assuming no oscillations) after 10 calendar years of data taking for $\bar{\nu}_e$ appearance, ν_e disappearance, and ν_μ disappearance, taking into account the expected backgrounds. Also shown are the corresponding probabilities for no oscillations.	67
11.1	A breakdown of the OscSNS cost estimate, including contingency and escalation. The OscSNS construction is assumed to start in the beginning of FY15 and last for 3 years.	74

List of Figures

2.1	The probability of $\bar{\nu}_\mu \rightarrow \bar{\nu}_e$ from LSND and $\bar{\nu}_\mu \rightarrow \bar{\nu}_e$ and $\nu_\mu \rightarrow \nu_e$ from MiniBooNE as a function of the neutrino proper time.	13
2.2	A global fit to the world neutrino plus antineutrino data indicates that the world data fit reasonably well to a 3+2 model with three active neutrinos plus two sterile neutrinos [7]. . .	14
2.3	The OscSNS sensitivity curves for the simulated sensitivity to $\bar{\nu}_\mu \rightarrow \bar{\nu}_e$ oscillations after two (left) and six (right) <i>calendar</i> years of operation, assuming a 50% beam on-time (one and three years of running at 100% beam-on). Note that it has more than 5σ sensitivity to the LSND result in 2 years.	15
2.4	The OscSNS sensitivity curves for ν_μ disappearance for two and six <i>calendar</i> years, respectively.	15
2.5	The expected oscillation probability from $\bar{\nu}_e$ appearance as a function of L/E for $\sin^2 2\theta = 0.005$ and $\Delta m^2 = 1 \text{ eV}^2$ (left plot) and $\Delta m^2 = 4 \text{ eV}^2$ (right plot). The plot assumes ten calendar years of data collection at 50% beam live-time.	16
4.1	The neutrino time and energy spectra of the different neutrino species produced isotropically from a stopped pion source [8].	22
4.2	A photograph of the completed SNS facility.	23
4.3	Plan view of the SNS facility. The proposed second target hall is located in the right portion of the view.	24
4.4	Perspective view of the target station.	25
4.5	An enlargement of the mercury target.	26
4.6	The time distribution of a typical beam pulse, where the vertical axis is the current in Amperes and the horizontal axis is the time in units of 10 ns.	27
5.1	A cut-away schematic drawing of the OscSNS cylindrical detector tank.	29
5.2	A photograph of the suggested detector location in relation to the SNS target hall.	30
5.3	A schematic drawing of the suggested detector location in relation to the SNS target hall. . .	31

5.4	A schematic drawing of the suggested detector location in relation to the SNS target hall. Dirt provides the overburden for this design.	32
5.5	A cut-away schematic drawing of the detector hall.	33
5.6	A cut-away schematic drawing of the electronics area above the detector tank.	34
6.1	A schematic drawing of the detector location in relation to the SNS target hall.	42
6.2	Time spectra of negative muons in various materials.	43
6.3	Energy spectra of neutrinos produced from the decay of pions and muons at the SNS. From left to right, top: $\nu_\mu, \bar{\nu}_\mu$; bottom: $\nu_e, \bar{\nu}_e$. Rates are for 50M protons on target. The prominent feature in the ν_μ spectra around 90 MeV comes from the muMinusCaptureAtRest process in Geant4.	44
6.4	Time spectra corresponding to Figure 6.3. From left to right, top: $\nu_\mu, \bar{\nu}_\mu$; bottom: $\nu_e, \bar{\nu}_e$. Rates are for 50M protons on target.	45
6.5	Angular distributions for muon neutrinos (left) and anti-neutrinos (right), from all decays in flight of positive and negative pions, respectively. The angle is taken between the emitted neutrino direction and the direction to the detector. Rates are for 50M protons on target. . .	46
8.1	The separation of electrons and protons that was achieved with the LSND experiment [2]. . .	52
9.1	Input cross sections as a function of incident neutrino energy. Cross section plots include a 5% uncertainty. From left to right, top: $\nu \ ^{12}\text{C} \rightarrow \ ^{12}\text{C}^*$, $\bar{\nu} \ ^{12}\text{C} \rightarrow \ ^{12}\text{C}^*$; middle: $\bar{\nu}_e \ ^{12}\text{C} \rightarrow e^+ \ ^{12}\text{B}$, $\bar{\nu}_e \ p \rightarrow e^+ \ n$; bottom: $\nu_e \ ^{12}\text{C} \rightarrow e^- \ ^{12}\text{N}$	55
9.2	Input flux as a function of incident neutrino energy, for neutrinos reaching the detector. These plots include neutrinos from DAR and DIF. From left to right, top: $\nu_\mu, \bar{\nu}_\mu$; bottom: $\nu_e, \bar{\nu}_e$. Rates are for 50M simulated protons on target.	56
9.3	The KARMEN measurement of $\nu_\mu \ ^{12}\text{C} \rightarrow \nu_\mu \ ^{12}\text{C}^*$, where the shaded region corresponds to the fast neutron background and the hatched region corresponds to the neutrino and cosmic ray backgrounds. The right plot shows the background subtracted signal.	59
9.4	OscSNS sensitivity for ν_μ disappearance, for two calendar years of run time (left), and six calendar years of run time (right).	59
9.5	OscSNS sensitivity for the total flux disappearance, for two calendar years of run time (left), and six calendar years of run time (right).	60
9.6	The measurement of the reaction $\nu_e \ ^{12}\text{C} \rightarrow e^- \ ^{12}\text{N}_{gs}$ by the LSND experiment. The background, which is estimated to be $\sim 1\%$, is shown as the dotted curve.	61
9.7	OscSNS sensitivity for $\bar{\nu}_\mu \rightarrow \bar{\nu}_e$ oscillations, for two calendar years of run time (left), and six calendar years of run time (right).	62

9.8	OscSNS sensitivity for $\nu_\mu \rightarrow \nu_e$ oscillations, for two calendar years of run time (left), and six calendar years of run time (right).	63
10.1	The expected oscillation probability from $\bar{\nu}_e$ appearance as a function of L/E for $\sin^2 2\theta = 0.005$ and $\Delta m^2 = 1 \text{ eV}^2$, for ten <i>calendar</i> years of data collection at 50% beam live-time. . . .	68
10.2	The expected oscillation probability from $\bar{\nu}_e$ appearance as a function of L/E for $\sin^2 2\theta = 0.005$ and $\Delta m^2 = 4 \text{ eV}^2$, for ten <i>calendar</i> years of data collection at 50% beam live-time. . . .	69
10.3	The expected probability for ν_μ to remain a ν_μ as a function of L/E for $\sin^2 2\theta = 0.15$ and $\Delta m^2 = 1 \text{ eV}^2$, for ten <i>calendar</i> years of data collection at 50% beam live-time.	70
10.4	The expected probability for ν_μ to remain a ν_μ as a function of L/E for $\sin^2 2\theta = 0.15$ and $\Delta m^2 = 4 \text{ eV}^2$, for ten <i>calendar</i> years of data collection at 50% beam live-time.	71
10.5	The expected probability for ν_e to remain a ν_e as a function of L/E for $\sin^2 2\theta = 0.15$ and $\Delta m^2 = 1 \text{ eV}^2$, for ten <i>calendar</i> years of data collection at 50% beam live-time.	72
10.6	The expected probability for ν_e to remain a ν_e as a function of L/E for $\sin^2 2\theta = 0.15$ and $\Delta m^2 = 4 \text{ eV}^2$, for ten <i>calendar</i> years of data collection at 50% beam live-time.	73

Chapter 1

Executive Summary

There exists a need to address and resolve the growing evidence for short-baseline neutrino oscillations and the possible existence of sterile neutrinos. Such non-standard particles require a mass of $\sim 1 \text{ eV}/c^2$, far above the mass scale associated with active neutrinos, and were first invoked to explain the LSND $\bar{\nu}_\mu \rightarrow \bar{\nu}_e$ appearance signal [2]. More recently, the MiniBooNE experiment has reported a 2.8σ excess of events in antineutrino mode consistent with neutrino oscillations and with the LSND antineutrino appearance signal [3]. MiniBooNE also observed a 3.4σ excess of events in their neutrino mode data. Lower than expected neutrino-induced event rates using calibrated radioactive sources [4] and nuclear reactors [5] can also be explained by the existence of sterile neutrinos. Fits to the world's neutrino and antineutrino data are consistent with sterile neutrinos at this $\sim 1 \text{ eV}/c^2$ mass scale, although there is some tension between measurements from disappearance and appearance experiments [6, 7]. In addition to resolving this potential major extension of the Standard Model, the existence of sterile neutrinos will impact design and planning for all future neutrino experiments. It should be an extremely high priority to conclusively establish if such unexpected light sterile neutrinos exist. **The Spallation Neutron Source (SNS) at Oak Ridge National Laboratory [8], built to usher in a new era in neutron research, provides a unique opportunity for US science to perform a definitive world-class search for sterile neutrinos.**

The 1.4 MW beam power of the SNS is a prodigious source of neutrinos from the decay of π^+ and μ^+ at rest. These decays produce a well specified flux of neutrinos via $\pi^+ \rightarrow \mu^+ \nu_\mu$, $\tau_\pi = 2.7 \times 10^{-8} \text{ s}$, and $\mu^+ \rightarrow e^+ \nu_e \bar{\nu}_\mu$, $\tau_\mu = 2.2 \times 10^{-6} \text{ s}$. The low duty factor of the SNS ($\sim 695 \text{ ns}$ beam pulses at 60 Hz , $DF = 4.2 \times 10^{-5}$) is more than 1000 times less than LAMPF. This much smaller duty factor provides a reduction in backgrounds due to cosmic rays, and allows the ν_μ induced events from π^+ decay to be separated from the ν_e and $\bar{\nu}_\mu$ induced events from μ^+ decay.

The OscSNS experiment will make use of this prodigious source of neutrinos. The OscSNS detector will be centered 60 meters from the SNS target, in the backward direction. The cylindrical detector design is based upon the LSND and MiniBooNE detectors and will consist of an 800-ton tank of mineral oil with a small concentration of b-PBD scintillator dissolved in the oil, that is covered by approximately 3500 8-inch phototubes for a photocathode coverage of 25%. The cylindrical design will allow us to map the event rates as a function of L/E , to look for any sinusoidal dependence indicative of oscillations.

This experiment will use the mono-energetic 29.8 MeV ν_μ to investigate the existence of light sterile neutrinos via the neutral-current reaction $\nu_\mu C \rightarrow \nu_\mu C^*(15.11\text{MeV}) \rightarrow \nu_\mu C \gamma$. This reaction has the same cross section for all active neutrinos, but is zero for sterile neutrinos. An observed oscillation in this reaction is direct evidence for sterile neutrinos. OscSNS can also carry out a unique and decisive test of the LSND $\bar{\nu}_\mu \rightarrow \bar{\nu}_e$ appearance signal. In addition, OscSNS can make a sensitive search for ν_e disappearance by searching for oscillations in the reaction $\nu_e C \rightarrow e^- N_{gs}$, where the N_{gs} is identified by its beta decay. It is important to note that all cross sections involved are known to two percent or better.

The SNS represents a unique opportunity to pursue a critical neutrino physics program in a cost-effective manner, as an intense flux of neutrinos from stopped π^+ and μ^+ decay are produced during normal SNS operations. The existence of light sterile neutrinos would be the first major extension of the Standard Model. Sterile neutrino properties are central to dark matter, cosmology, astrophysics, and future neutrino research. **The OscSNS experiment would be able to prove whether sterile neutrinos can explain these existing short-baseline anomalies.**

Chapter 2

Physics Goals

Observations of neutrino oscillations, and therefore neutrino mass, have been made by solar-neutrino experiments at a $\Delta m^2 \sim 8 \times 10^{-5} \text{ eV}^2$, and by atmospheric-neutrino experiments at a $\Delta m^2 \sim 3 \times 10^{-3} \text{ eV}^2$, where Δm^2 is the difference in mass squared of the two dominant mass eigenstates contributing to the oscillations [1]. In addition to these observations, the LSND experiment, which took data at Los Alamos National Laboratory (LANSCE) for six years from 1993 to 1998, obtained evidence for $\bar{\nu}_\mu \rightarrow \bar{\nu}_e$ oscillations at a $\Delta m^2 \sim 1 \text{ eV}^2$ [2]. Oscillations at the mass splittings seen by LSND do not fit with well-established oscillation observations from solar and atmospheric experiments. The Standard Model, with only three flavors of neutrinos, cannot accommodate all three observations. Confirmation of LSND-style oscillations would require further non-trivial extensions to the Standard Model.

The MiniBooNE experiment at Fermilab, designed to search for $\nu_\mu \rightarrow \nu_e$ and $\bar{\nu}_\mu \rightarrow \bar{\nu}_e$ oscillations and to further explore the LSND neutrino oscillation evidence, has presented separate neutrino and antineutrino oscillation results. Combining these results, MiniBooNE observes a 3.8σ excess of events in the 200-1250 MeV oscillation energy range that is consistent with the LSND signal [9, 3]. Many of the beyond the Standard Model explanations of this excess involve sterile neutrinos, which would have a huge impact on astrophysics, supernovae neutrino bursts, dark matter, and the creation of the heaviest elements. Fig. 2.1 shows the L/E (neutrino proper time) dependence of $\bar{\nu}_\mu \rightarrow \bar{\nu}_e$ from LSND and $\bar{\nu}_\mu \rightarrow \bar{\nu}_e$ and $\nu_\mu \rightarrow \nu_e$ from MiniBooNE. The correspondence between the two experiments is striking. Furthermore, Fig. 2.2 shows fits to the world neutrino plus antineutrino data that indicate that the world data fit reasonably well to a 3+2 model with three active neutrinos and two sterile neutrinos [7].

The SNS [8] offers many advantages for neutrino oscillation physics, including known neutrino spectra, well understood neutrino cross sections (uncertainties less than a few percent), low duty factor for cosmic ray background rejection, low beam-induced neutrino background, and a very high neutrino rate of greater than $10^{15}/\text{s}$ from the decay of stopped pions and muons in the Hg beam dump. Stopped pions produce 29.8 MeV mono-energetic ν_μ from $\pi^+ \rightarrow \mu^+ \nu_\mu$ decay, while stopped muons produce $\bar{\nu}_\mu$ and ν_e up to the 52.8 MeV endpoint from $\mu^+ \rightarrow e^+ \nu_e \bar{\nu}_\mu$ decay. Note that greater than 99% of π^- and μ^- capture in Hg before they have a chance to decay, so that hardly any neutrinos are produced from either $\pi^- \rightarrow \mu^- \bar{\nu}_\mu$ or $\mu^- \rightarrow e^- \bar{\nu}_e \nu_\mu$ decay.

The SNS neutrino flux is good for probing $\bar{\nu}_\mu \rightarrow \bar{\nu}_e$ and $\nu_\mu \rightarrow \nu_e$ appearance, as well as ν_μ and ν_e disappearance into sterile neutrinos. The appearance searches both have a two-fold coincidence for the rejection of background. For $\bar{\nu}_\mu \rightarrow \bar{\nu}_e$ appearance, the signal is an e^+ in coincidence with a 2.2 MeV γ : $\bar{\nu}_e p \rightarrow e^+ n$, followed by $np \rightarrow D\gamma$. For $\nu_\mu \rightarrow \nu_e$ appearance, the signal is a mono-energetic 12.5 MeV e^- in coincidence with an e^+ from the β decay of the ground state of ^{12}N : $\nu_e ^{12}\text{C} \rightarrow e^- ^{12}\text{N}_{gs}$, followed by $^{12}\text{N}_{gs} \rightarrow ^{12}\text{C}e^+\nu_e$. The ν_μ disappearance search will detect the prompt 15.11 MeV γ from the neutral-current reaction $\nu_\mu C \rightarrow \nu_\mu C^*$ (15.11). This reaction has been measured by the KARMEN experiment, which has determined a cross section that is consistent with theoretical expectations [10]. However, the KARMEN result was measured in a sample of 86 events, and carries a 20% total error. OscSNS will be able to greatly improve upon the statistical and systematic uncertainties of this measurement. If OscSNS observes an event rate from this neutral-current reaction that is less than expected, or if the event rate displays a sinusoidal dependence with distance (L/E can be measured with a resolution of $\sim 1\%$), then this will be evidence for ν_μ oscillations into sterile neutrinos. The ν_e disappearance search will measure the reaction $\nu_e C \rightarrow e^- N_{gs}$ followed by N_{gs} beta decay. This reaction is very clean with a very low background due to the two-fold signature. Furthermore, the neutrino energy is approximately equal to the electron energy, so that L/E can be measured with a resolution of $< 5\%$, which allows for a sensitive test for oscillations in the detector.

In addition to the neutrino oscillation searches, OscSNS will also make precision cross section measurements of $\nu_e C \rightarrow e^- N_{gs}$ scattering and $\nu e^- \rightarrow \nu e^-$ elastic scattering. The former reaction has a well-understood cross section and can be used to normalize the total neutrino flux, while the latter reaction, involving ν_μ , ν_e , and $\bar{\nu}_\mu$, will allow a precision measurement of $\sin^2 \theta_W$.

Table 2.1 summarizes the expected event sample sizes for the disappearance and appearance oscillation searches, per calendar year, at the OscSNS. Figure 2.3 shows the expected sensitivity for $\bar{\nu}_e$ appearance after two and six calendar years of run time, while Figure 2.4 presents the sensitivity for ν_μ disappearance. The LSND allowed region is fully covered by more than 5σ . The cylindrical design of the OscSNS detector allows for detection of oscillations as a function of L/E , as shown in Figure 2.5. Such an observation would prove that any observed excess is due to short-baseline neutrino oscillations, and not due to a misunderstood background. The oscillation sensitivities are further improved by the construction of a near detector and by the planned construction of a second target station that is located at a longer neutrino baseline.

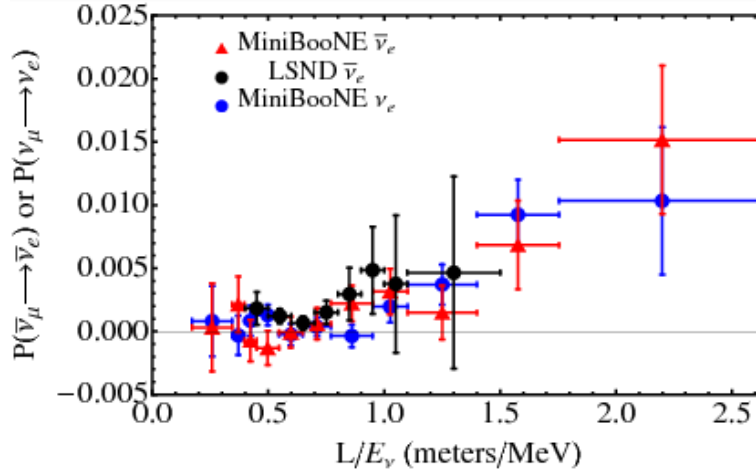


Figure 2.1: The probability of $\bar{\nu}_\mu \rightarrow \bar{\nu}_e$ from LSND and $\bar{\nu}_\mu \rightarrow \bar{\nu}_e$ and $\nu_\mu \rightarrow \nu_e$ from MiniBooNE as a function of the neutrino proper time.

Channel	Background	Signal
Disappearance Search		
$\nu_\mu \ ^{12}\text{C} \rightarrow \nu_\mu \ ^{12}\text{C}^*$		
$\nu_e \ ^{12}\text{C} \rightarrow \nu_e \ ^{12}\text{C}^*$		
$\bar{\nu}_\mu \ ^{12}\text{C} \rightarrow \bar{\nu}_\mu \ ^{12}\text{C}^*$	1060 ± 36	3535 ± 182
$\nu_\mu \ ^{12}\text{C} \rightarrow \nu_\mu \ ^{12}\text{C}^*$	224 ± 75	745 ± 42
$\nu_e \ ^{12}\text{C} \rightarrow e^- \ ^{12}\text{N}_{gs}$	24 ± 13	2353 ± 123
Appearance Search		
$\bar{\nu}_\mu \rightarrow \bar{\nu}_e: \bar{\nu}_e \ ^{12}\text{C} \rightarrow e^+ \ ^{11}\text{B} \ n$		
$\bar{\nu}_\mu \rightarrow \bar{\nu}_e: \bar{\nu}_e \ p \rightarrow e^+ \ n$	42 ± 5	120 ± 10
$\nu_\mu \rightarrow \nu_e: \nu_e \ ^{12}\text{C} \rightarrow e^- \ ^{12}\text{N}_{gs}$	12 ± 3	3.5 ± 1.5

Table 2.1: Summary of per calendar year event rate predictions for a detector located at the SNS, centered at a distance of 60 meters from the interaction point, at ~ 150 degrees in the backward direction from the proton beam. The first column is the oscillation channel, the second column is the expected intrinsic background, and the third column is the expected signal for appearance searches and the total number of events for disappearance searches. All event rates account for a 50% detector efficiency, a 50% beam-on efficiency, a fiducial volume of 523 m^3 , and are in units of expected events per calendar year. Appearance signal estimates assume a 0.26% oscillation probability.

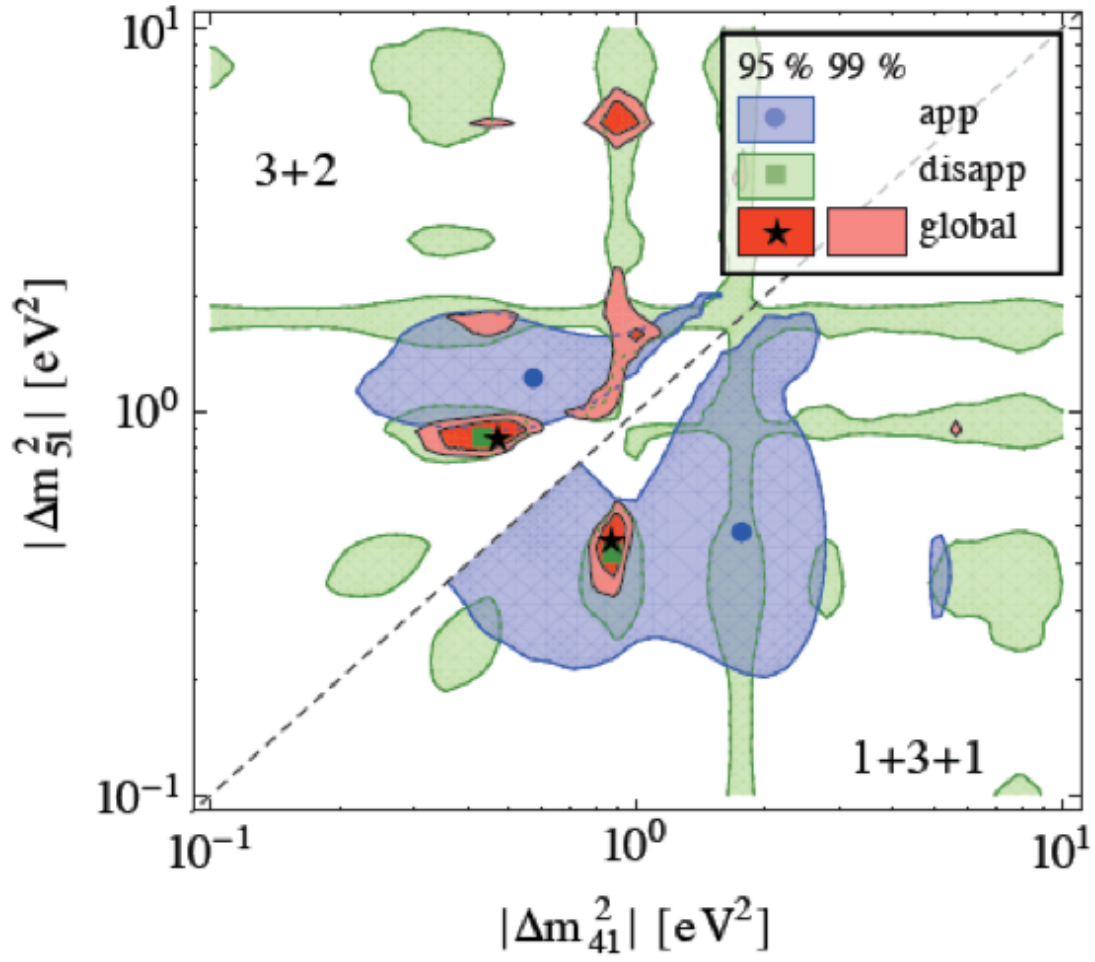


Figure 2.2: A global fit to the world neutrino plus antineutrino data indicates that the world data fit reasonably well to a 3+2 model with three active neutrinos plus two sterile neutrinos [7].

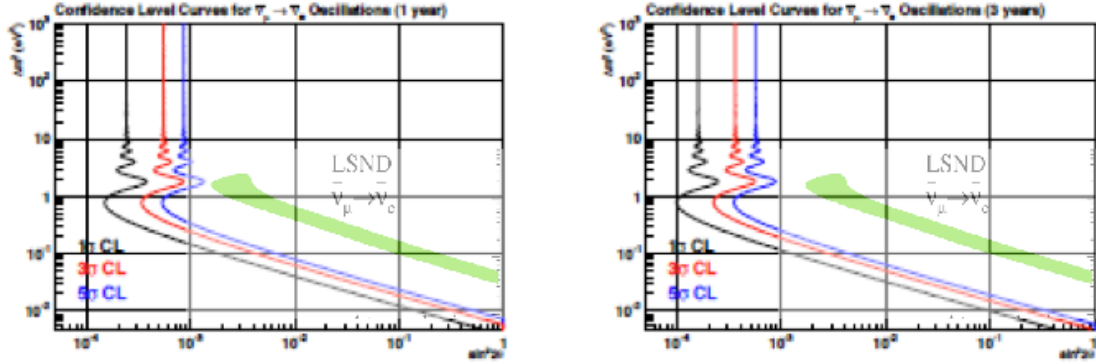


Figure 2.3: The OscSNS sensitivity curves for the simulated sensitivity to $\bar{\nu}_\mu \rightarrow \bar{\nu}_e$ oscillations after two (left) and six (right) *calendar* years of operation, assuming a 50% beam on-time (one and three years of running at 100% beam-on). Note that it has more than 5σ sensitivity to the LSND result in 2 years.

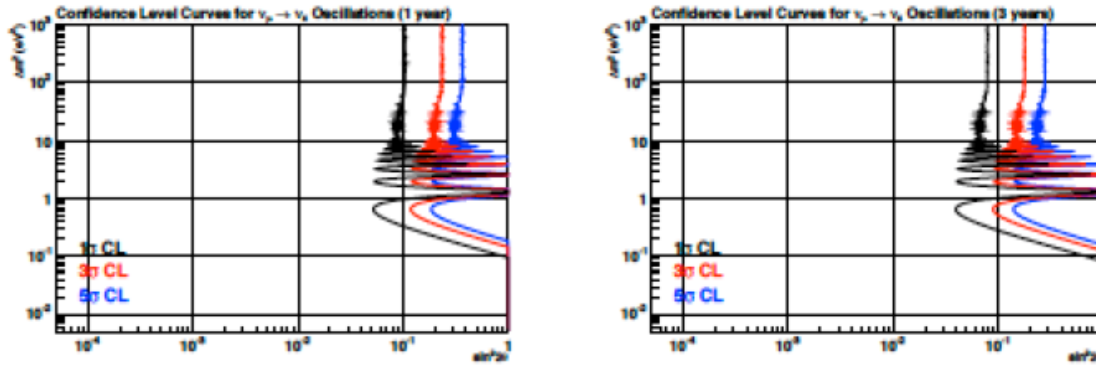


Figure 2.4: The OscSNS sensitivity curves for ν_μ disappearance for two and six *calendar* years, respectively.

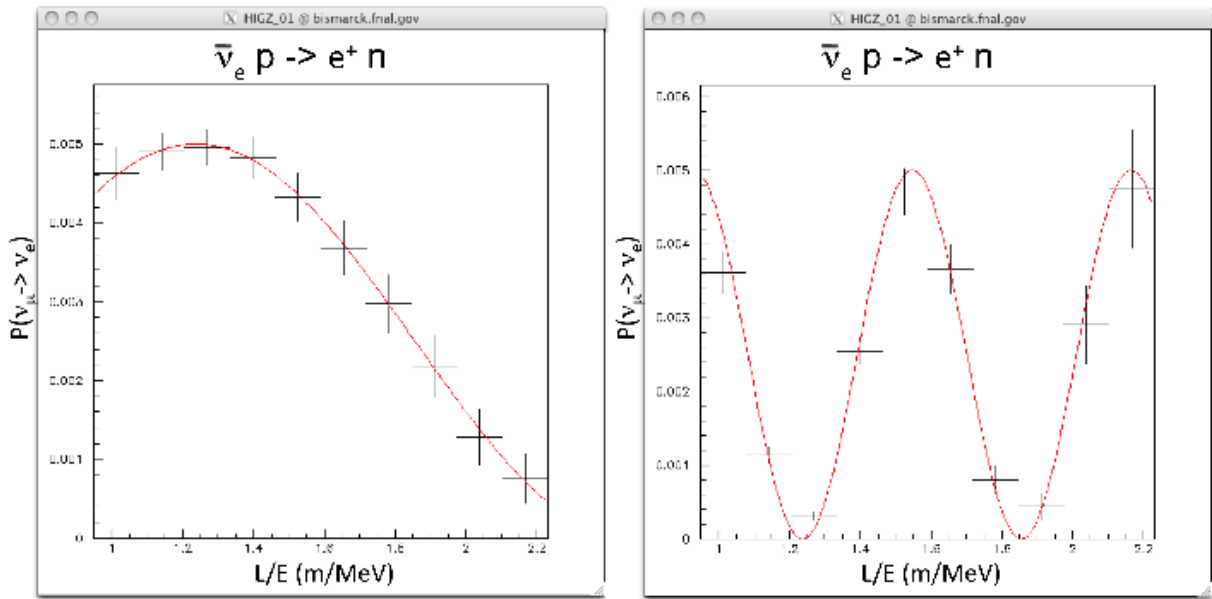


Figure 2.5: The expected oscillation probability from $\bar{\nu}_e$ appearance as a function of L/E for $\sin^2 2\theta = 0.005$ and $\Delta m^2 = 1 \text{ eV}^2$ (left plot) and $\Delta m^2 = 4 \text{ eV}^2$ (right plot). The plot assumes ten calendar years of data collection at 50% beam live-time.

Chapter 3

Path to Funding

The OscSNS experiment is proposing to operate at the SNS, a laboratory currently funded under Basic Energy Sciences (BES). There isn't a strong history of funding at Oak Ridge by the High Energy Physics (HEP) program, and that makes our path forward for requesting funding less straight forward. This chapter describes our justification for running at Oak Ridge, and the path we propose to take to achieve full funding.

3.1 Why the SNS?

There are currently 8 national laboratories that have or are seeking funding from the Department of Energy High Energy Physics Intensity Frontier (DOE HEP IF) program. Due to funding challenges, it is valid to question why we are seeking to open another laboratory for DOE HEP funding, instead of proposing our experiment at a lab that is already being funded under this program. The simple answer to this question is two-fold. The neutrinos at the SNS come for free, as they are created during the process that produces the spallation neutrons. This dramatically increases the cost effectiveness of the experiment and provides “more bang for your buck” than can be had at any other facility. Also, the energy spectrum of the neutrino beam provides a golden opportunity for precision short-baseline neutrino experiments and the possible discovery of sterile neutrinos. Due to the low-energy neutrinos from stopped π^+ and μ^+ decays, the OscSNS experiment has the potential of actually observing oscillations in the detector from both charged-current and neutral-current interactions, definitively proving the existence of sterile neutrinos. This is not possible at a higher energy neutrino source, where the parent pions and muons decay in flight.

3.1.1 SNS vs FNAL facilities

FNAL provides high-energy neutrinos from π^+ and K^+ decay in flight (DIF) that are ideal for long-baseline neutrino experiments at the atmospheric neutrino mass scale of $\Delta m^2 \sim 2 \times 10^{-3} \text{ eV}^2$. However, for short-baseline neutrino experiments at a mass scale of $\Delta m^2 \sim 1 \text{ eV}^2$, there is a clear advantage in using neutrinos from π^+ and μ^+ decay at rest (DAR). For DAR neutrino sources, the neutrino energy spectra are

known perfectly, the neutrino cross section uncertainties are $< 2\%$, and the low neutrino energies allow the possibility of actually observing an oscillation pattern of event rates in the detector.

FNAL has two running neutrino beamlines: the NuMI beamline, and the Booster beamline (BNB). Both of these are DIF neutrino sources with a peak energy of 700 MeV (BNB) and 4 GeV (NuMI). In the BNB beam stop there are also neutrinos produced from π^+ and μ^+ decay at rest. There are several factors that make this a far less attractive DAR source. The proton beam power at FNAL is 30 kW, compared to the 1400 kW of the SNS. As pion production, and therefore neutrino production, is roughly proportional to beam power, this results in a far less intense neutrino beam for a detector placed 60 meters away from the beam stop. The identification of an oscillatory pattern in event rates is crucial for definitively claiming discovery of sterile neutrinos. The oscillation pattern will only be apparent in the detector if the neutrino production region is small. At FNAL, the pions and muons flying through the air come to rest in the beam stop located 50 meters from the proton-Be target region, in addition to coming to rest near the Be target and along the walls of the 50 meter decay pipe. This results in the spreading out of the DAR neutrino beam. Use of the Booster DAR neutrino source will tend to wash out any oscillation pattern and will result in an experiment that will observe an excess or deficit of events, but that will be unable to conclusively observe oscillations to sterile neutrinos. Compare this to the SNS, where pions produced in the proton-Hg interaction are immediately brought to rest inside of the target (at $>99\%$). Thus, the uncertainty of the neutrino production location at the SNS is limited to the size of the Hg target, or ~ 50 cm.

However, the results found by OscSNS will directly and positively impact the Intensity Frontier program at Fermilab. The resolution to the hints of physics beyond the Standard Model in the neutrino sector will dramatically impact the program plan at Fermilab, allowing them to best choose next generation experiments to either elucidate further the properties of the sterile neutrino, or to pursue other Intensity Frontier goals should the existence of sterile neutrinos at this energy scale be disproven.

3.1.2 SNS vs All Other World Facilities

The only other world facility that is comparable to the SNS is the J-PARC spallation source in Japan, which has similar proton beam power (1.0 MW for J-PARC vs. 1.4 MW for SNS). J-PARC has the advantage of a lower duty factor (5×10^{-6} for J-PARC vs. 42×10^{-6} for SNS), while the SNS has the advantage of a lower proton beam energy (3 GeV for J-PARC vs. 1 GeV for SNS). The lower proton energy is desirable due to the lack of backgrounds from produced kaons and a lower energy neutron background. The lower energy proton beam at the SNS will cause more of the produced pions to come to rest inside the target, resulting in a smaller size of the neutrino source. As mentioned above, the smaller the neutrino source the more clearly the pattern of oscillations to sterile neutrinos can be distinguished in the detector.

3.2 Why OscSNS is Unique

OscSNS is a unique experiment that will make full use of the capabilities of the SNS facility. With OscSNS, the neutrino energy spectra are known perfectly, the neutrino oscillation channel cross section uncertainties are $< 2\%$, there is no bias from nuclear effects in the determination of neutrino energy, the intrinsic $\bar{\nu}_e$ background is very low at the level of 0.1%, and the potential exists to observe short-baseline oscillations in the detector for both charged-current and neutral-current interactions to prove (or disprove)

the existence of sterile neutrinos. OscSNS will have excellent sensitivity for $\bar{\nu}_\mu \rightarrow \bar{\nu}_e$ appearance, as well as ν_e and ν_μ disappearance. Overall, OscSNS will be able to make a definitive test of the current evidence for short-baseline neutrino oscillations, which imply the existence of physics beyond the Standard Model.

3.2.1 Complementariness to Other Experiments

OscSNS is complementary to the MicroBooNE and NuSTORM experiments at FNAL and to other short-baseline experiments around the world (IsoDAR). If light sterile neutrinos exist in nature, then it will be important to confirm the oscillation signal in a variety of experiments at different energy scales, especially if there are two or more types of sterile neutrinos and short-baseline CP violation. MicroBooNE will play an important role in determining whether the excess of events observed by MiniBooNE is due to electron events or photon events; however, MicroBooNE by itself will not be able to prove whether there are short-baseline neutrino oscillations and sterile neutrinos. Additionally, IsoDAR will only be able to observe oscillations in the CC channel; they will be unable to measure NC scattering, the smoking gun for sterile neutrinos vs some other anomalous oscillation theory.

The OscSNS experiment is an order of magnitude less expensive and can be built more quickly than NuSTORM [11]. Indeed, if OscSNS proves the existence of sterile neutrinos, then these results will provide stronger motivation for building NuSTORM (as well as Project X). When comparing OscSNS and NuSTORM, it is important to compare the energy spectrum of the neutrino beam as well as the detector technology. NuSTORM is proposing to use a DIF neutrino source, with a far detector composed of steel and scintillator. NuSTORM will not be able to observe oscillations of a neutral-current interaction, the golden channel for claiming observation of oscillations to sterile neutrinos. Furthermore, OscSNS will not be affected by nuclear effects in the reconstruction of neutrino energy, which is not the case for NuSTORM, and the OscSNS neutrino cross sections are all known to within 1-2%. Finally, the strongest argument for OscSNS when compared to NuSTORM, is that OscSNS will be a direct test of LSND. If the LSND signal is due to some exotic physics other than neutrino oscillations, such as Lorentz violation, then OscSNS will be able to discover this new physics. This may not possible with the NuSTORM experiment.

3.2.2 DOE Mission Need

The question of short-baseline oscillations and sterile neutrinos is one of the most pressing issues in neutrino physics today. Light, sterile neutrinos would have a big impact on high-energy physics, nuclear physics, and astrophysics, and would contribute to the dark matter of the universe. Furthermore, short-baseline oscillations would affect present and future long-baseline neutrino experiments. Therefore, OscSNS represents a unique opportunity to provide a definitive test of short-baseline oscillations and to prove the existence of sterile neutrinos in a timely manner.

3.3 Path to Funding

The SNS currently does not have facilities in place for acceptance of an LOI, or for presentation to a PAC, for non-neutron experiments. Therefore, we propose the following course of action:

- Visit SNS, present physics plan. (done: April 12, 2013)
- Attend Snowmass, garner support from the community. (done)
- Obtain letter of support from SNS management and have it sent to DOE. (done)
- Submit R&D proposals to DOE for the following ground work (Fall, 2013):
 - design new electronics
 - test oil and scintillators from various sources
 - develop simulations for the main detector, including reconstruction and particle ID algorithms
 - develop improved neutrino flux simulations
- Submit white paper to DOE.

Following the DOE Critical Decision Approval process, we believe this program will allow us to solidly argue for CD-0 and CD-1 approval.

Upon completion of the R&D program, we will include results from the R&D program into the white paper, producing a Technical Design Report. The TDR will be submitted to the DOE for consideration in the MIE funding process.

Chapter 4

The SNS Neutrino Source

To search for neutrino oscillations in the mass range $\Delta m^2 > 0.1 \text{ eV}^2$ requires an intense source of well characterized neutrinos. The decay of stopped pions from the 1.4 MW, 1.3 GeV, short duty-cycle SNS [8] proton beam provides such a source. Neutrinos from stopped pion decay have a well defined flux, well defined energy spectrum, and measurements of their interactions tend to have low background rates. The dominant decay scheme that produces neutrinos from a stopped pion source is

$$\pi^+ \rightarrow \mu^+ \nu_\mu, \quad \tau = 26 \text{ ns} \quad (4.1)$$

followed by

$$\mu^+ \rightarrow e^+ \bar{\nu}_\mu \nu_e, \quad \tau = 2.2 \text{ } \mu\text{s}. \quad (4.2)$$

The neutrinos from stopped π^- 's are highly suppressed because the negative pions are absorbed in the surrounding target material. Thus, neutrinos from the π^- decay chain are significantly depleted and can be estimated from the measured ν_μ , $\bar{\nu}_\mu$, and ν_e flux. Fig. 4.1 shows the neutrino time and energy spectra from the SNS stopped pion source. As shown in the right hand plot, the ν_μ energy is mono-energetic ($E_{\nu_\mu} = 29.8 \text{ MeV}$), while the $\bar{\nu}_\mu$ and ν_e have known Michel energy distributions with an end-point energy of 52.8 MeV. Furthermore, the left hand plot shows the SNS beam timing and the time distributions for the three neutrino species. With a simple beam-on timing cut, one can obtain a fairly pure ν_μ sample with only a 14% contamination of $\bar{\nu}_\mu$ and ν_e each. This remaining background is easily measured from the time distribution and subtracted.

The expected proton rate from the SNS of 2.2×10^{23} protons/yr, coupled with a yield of 0.12 neutrinos per proton, produces 2.8×10^{22} ν /yr for 100% operation efficiency. Furthermore, the SNS is planning a future upgrade that will deliver MW beams to two sources, providing an interesting experimental environment of multiple baselines with a single detector.

A key component of the neutrino oscillation measurement is the physical size of the stopped pion source, which adds an uncertainty to the neutrino path length. For the SNS, the compact liquid mercury target will contribute approximately 25 cm (FWHM), or $\sim 0.4\%$ to the neutrino path length uncertainty.

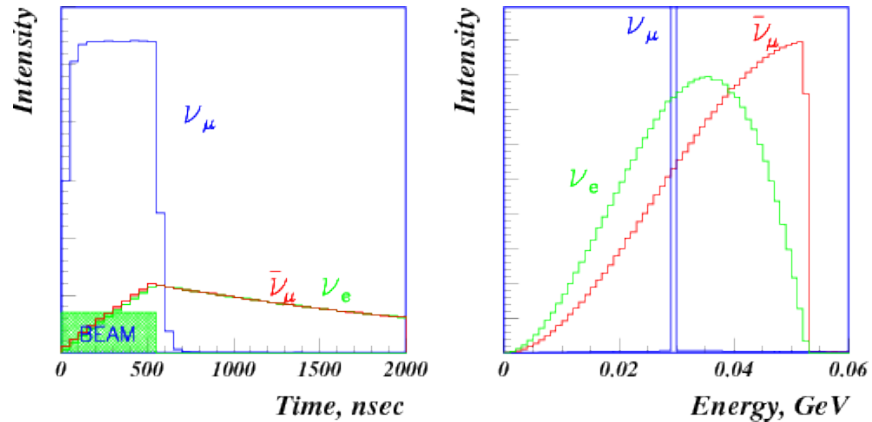


Figure 4.1: The neutrino time and energy spectra of the different neutrino species produced isotropically from a stopped pion source [8].

4.1 The Accelerator and the Target Station

The Spallation Neutron Source (SNS), now operating at the Oak Ridge National Laboratory, produces an intense 1.4 MW pulsed-proton beam. It consists of a 493 meter-long linac, an accumulator ring with a radius of just over 35 meters, and a target station. A second target station is planned in the future. The SNS is used primarily for material science research, however, it also is the world’s most intense accelerator neutrino source. The high intensity and the pulsed nature of the SNS provide an ideal laboratory for neutrino physics research at medium energies. The short-pulsed beam (695 ns, 60 Hz) provides a virtually cosmic-ray-free measurement of various neutrino interactions. It also provides the ability to distinguish between neutrinos from pion decay and muon decay. The only neutrino detector with this capability was the much smaller KARMEN experiment at the Rutherford Laboratory with significantly lower beam intensity (200 μ A).

A photograph of the completed SNS facility is shown in Fig. 4.2, while Fig. 4.3 shows a plan view of the facility. Note that in the plan view the future second target station is shown. It will have an intensity of 0.6 mA and repetition rate of 10 Hz. The two target stations will receive beams at different time slots. Table 4.1 shows the design parameters of the SNS.

Fig. 4.4 shows a cross section of the target station. A beam of protons enters from the lower left and strikes the target. The beam has a 7-cm by 20-cm spot size in order to reduce the local heat load in the target. The target, shown in Fig. 4.5, has dimensions of 40 cm by 10.4 cm by 50 cm. The mercury is contained within a multiple wall structure made of 316-type stainless steel. To remove heat, the mercury of the target is constantly circulated at the rate of 140 kg/sec. Room temperature moderators, filled with water, are placed under the target. Cryogenic liquid hydrogen moderators are located at the top. Target and moderators are surrounded by a lead reflector which extends at least to a radius of 1 meter around the target. All of this structure is encapsulated inside a thick steel vessel, to prevent neutrons from escaping into the experimental hall. There are 18 neutron channels looking at the moderators, rather than at the target. Shutters are provided on each channel.



Figure 4.2: A photograph of the completed SNS facility.

Fig. 4.6 shows the time distribution of a typical beam pulse, where the vertical axis is the current in Amperes and the horizontal axis is the time in units of 10 ns. The beam pulse has a total width of approximately 695 ns.

SNS Site Master Plan

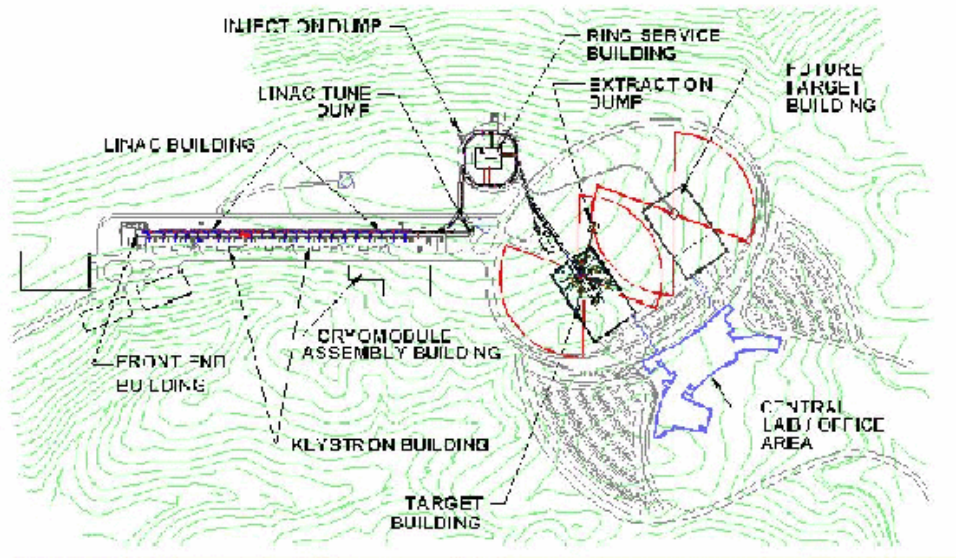


Figure 4.3: Plan view of the SNS facility. The proposed second target hall is located in the right portion of the view.

	baseline
linac length	493 m
accumulator ring circumference	221 m
beam power on the target	1.4 MW
beam energy on the target	1.3 GeV
average beam current	1.54 mA
repetition rate	60 Hz
ion type, source-linac	H^-
linac-beam duty factor	6.2%
number of injected turns	1225
particles stored in ring	1.5×10^{14}
extracted pulse length	695 nsec
peak current on target	45 A
target	mercury
beam spot on target	7×20 cm
moderators ambient	2 (water)
moderators cryogenic	2 (LH_2)
neutron beam ports	18

Table 4.1: SNS design parameters.

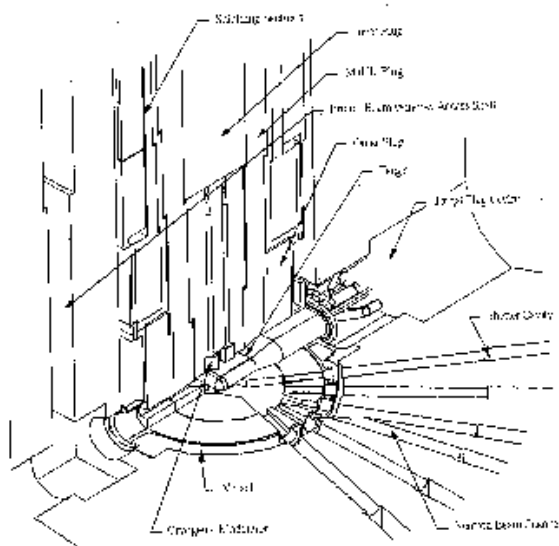


Figure 4.4: Perspective view of the target station.

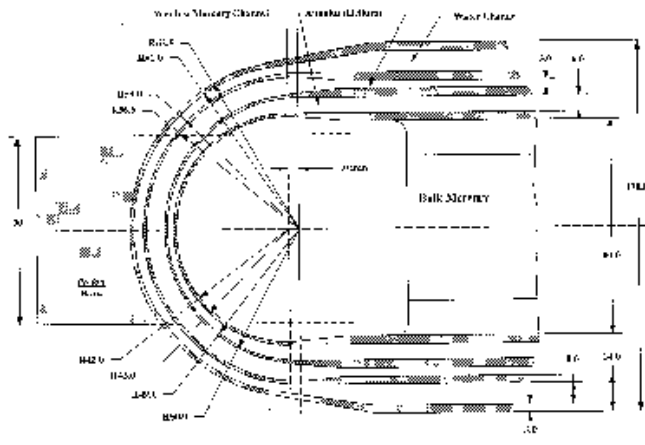


Figure 4.5: An enlargement of the mercury target.

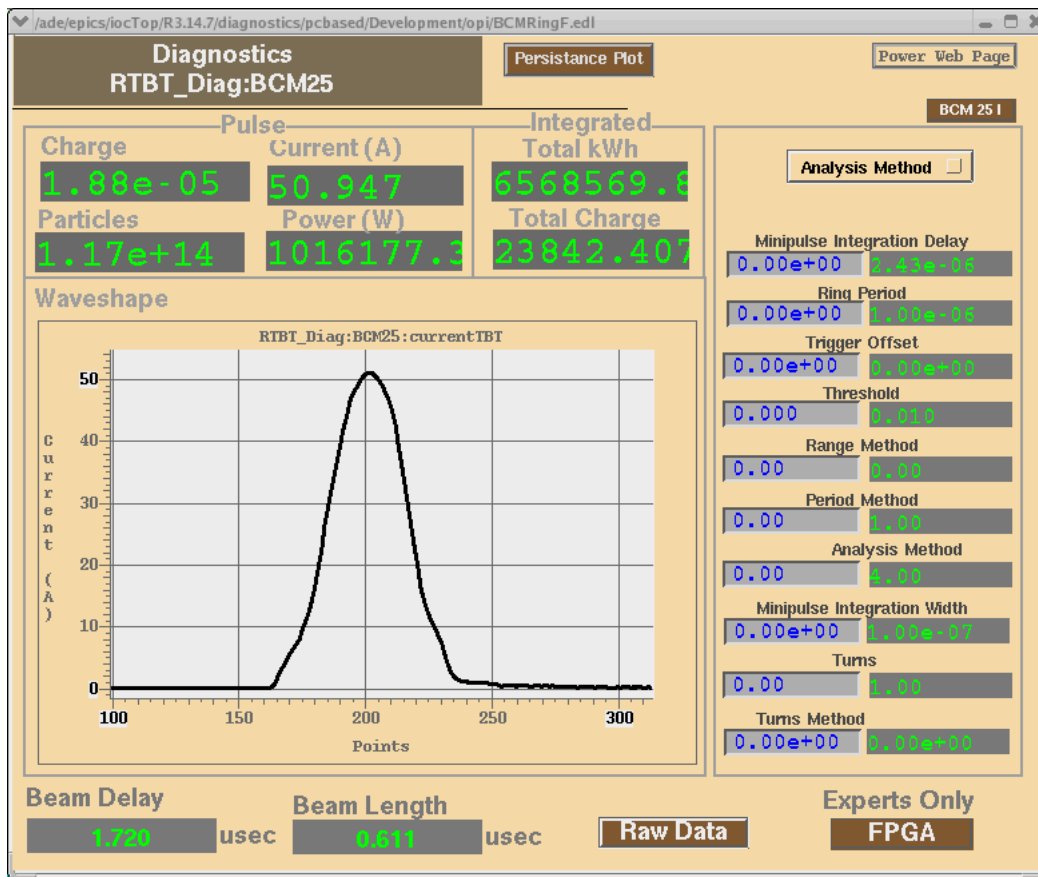


Figure 4.6: The time distribution of a typical beam pulse, where the vertical axis is the current in Amperes and the horizontal axis is the time in units of 10 ns.

Chapter 5

The OscSNS Detector

5.1 Overview

The OscSNS detector is a cylindrical detector, filled with mineral oil and lined with photomultiplier tubes, similar to the MiniBooNE detector at Fermilab. OscSNS differs from MiniBooNE in that it will have a higher phototube coverage and the addition of butyl-PBD scintillator to the mineral oil, ala LSND. Fig. 5.1 is a cut-away schematic drawing of the proposed detector, which consists of a 20.5 m long by 8 m diameter cylindrical tank lined with 4290 8-in phototubes at a radius of 3.5 m (3900 detector phototubes, corresponding to 25% coverage, and 390 veto phototubes, corresponding to 2.5% coverage). The detector is filled with 886 tonnes of mineral oil (density = 0.86), corresponding to a fiducial volume of 450 tonnes. Also, as in the LSND experiment [2], approximately 0.031 g/l (~ 30 kg) of butyl-PBD scintillator will be added to the mineral oil in order to increase the light output of low-energy particles and provide neutron detection.

The suggested location for the OscSNS detector is shown in Figure 5.2, where the center of the detector is located 60 m from the Hg beam dump at the SNS. By placing OscSNS somewhat upstream of the beam dump, the decay-in-flight neutrino background to the neutrino measurements will be negligible. The OscSNS detector will be buried under 6 m of dirt (or 2 m of steel) overburden, to provide shielding from cosmic rays and beam-induced neutrons. New electronics are being designed for OscSNS that will use ADCs with a faster clock speed than were used in LSND and MiniBooNE (200 MHz versus 10 MHz). Figures 5.4 and 5.3 show schematic drawings of the detector location in relation to the SNS target hall, while Figures 5.5 and 5.6 show schematic drawings of the electronics area above the detector tank.

The Detector Plant consists of two main elements: the Detector Containment and the Support Plant. The Detector Containment includes a cylindrical tank with access portal that sits in a rectangular vault. The Support Plant lies above the Detector Containment and includes area for tank access, utilities, and electronics.

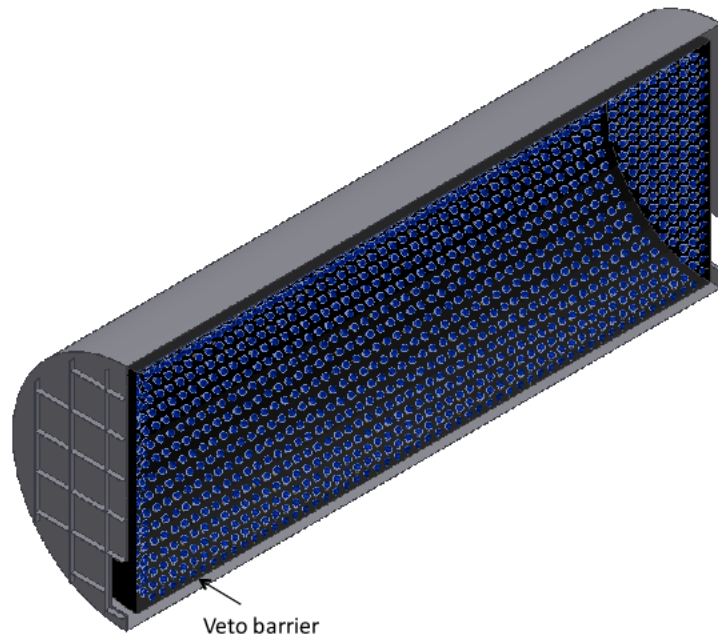


Figure 5.1: A cut-away schematic drawing of the OscSNS cylindrical detector tank.



Figure 5.2: A photograph of the suggested detector location in relation to the SNS target hall.

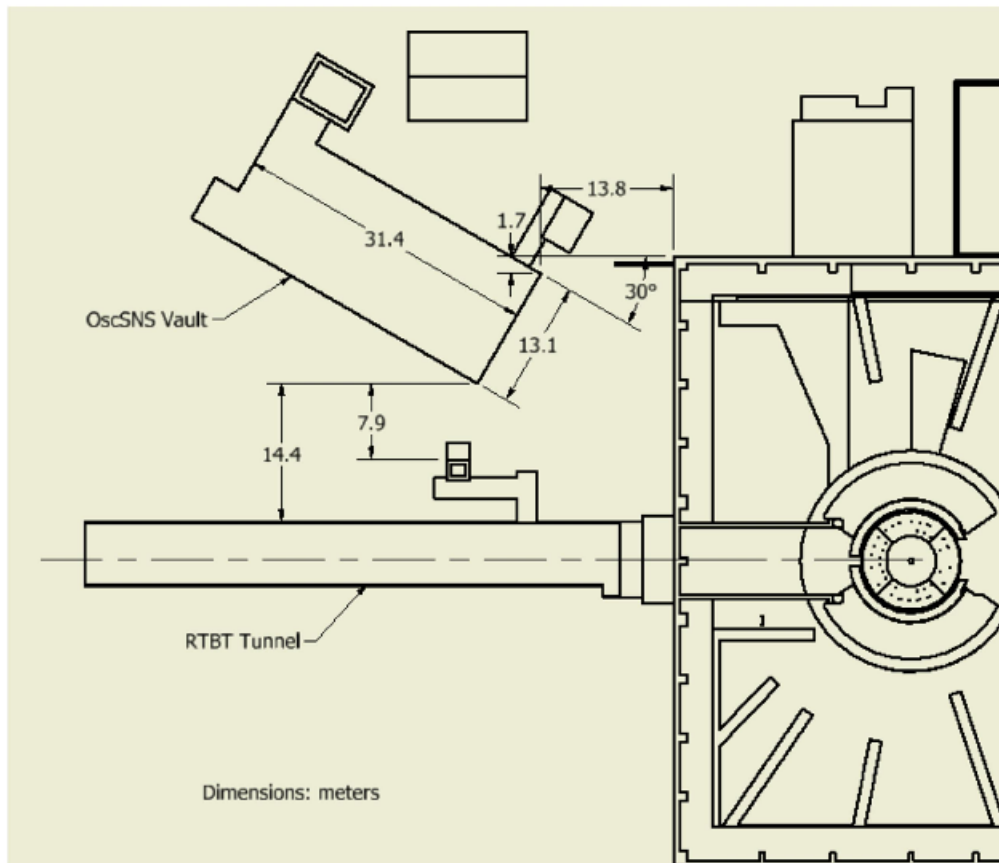


Figure 5.3: A schematic drawing of the suggested detector location in relation to the SNS target hall.



Figure 5.4: A schematic drawing of the suggested detector location in relation to the SNS target hall. Dirt provides the overburden for this design.

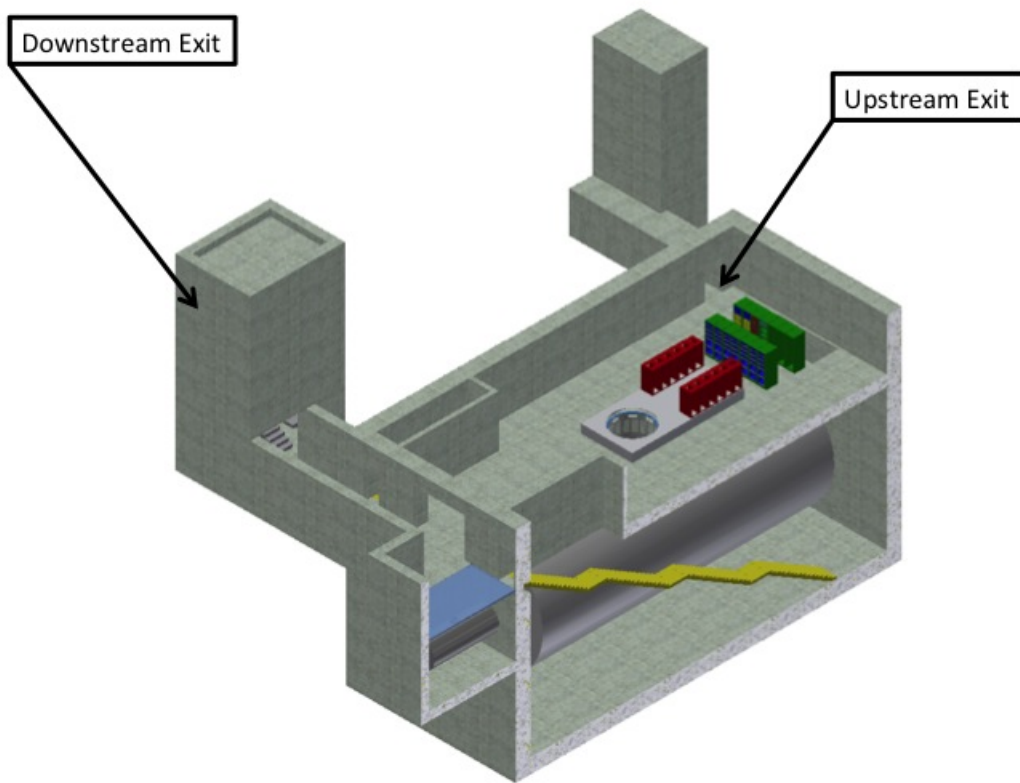


Figure 5.5: A cut-away schematic drawing of the detector hall.

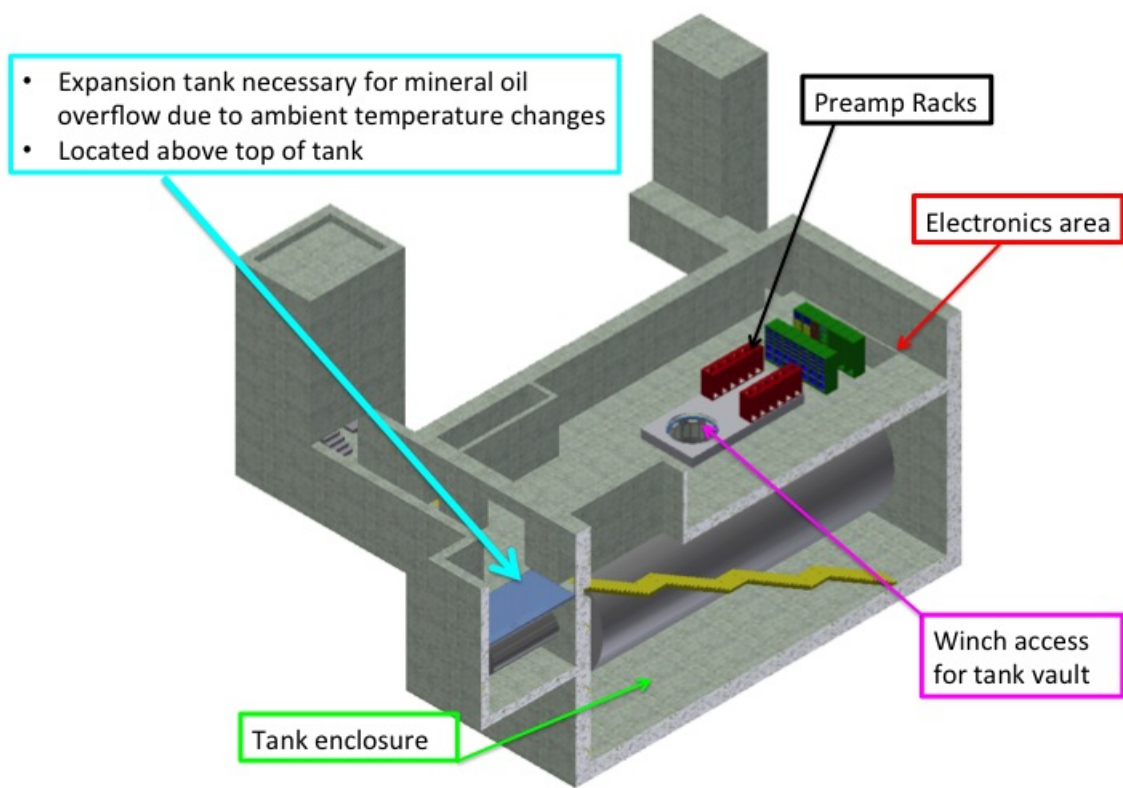


Figure 5.6: A cut-away schematic drawing of the electronics area above the detector tank.

5.2 Rectangular Vault

The rectangular vault will house the detector tank and will serve as the secondary containment for the oil. The vault will also provide the means for personnel access during the installation of phototubes. The excess soil from the excavation of the vault can be stored and reused as overburden for the detector enclosures to provide shielding from cosmic rays.

5.3 Cylindrical Tank

The cylindrical tank will have a diameter of 8 m, a length of 20.5 m, and will be constructed out of steel panels inside the rectangular vault. Bosses that will be used to support the phototube support structure and cable plant will be welded on the inside walls of the tank. An 8-foot diameter access portal is attached to the top of the tank and provides the principal means for equipment access. The diameter of the access portal is sufficient for all expected penetrations of the tank, including plumbing, cabling, and calibration lines. There will also be a personnel access port near the bottom of the tank. After the tank is filled with mineral oil, the oil level in the access portal will be stabilized below the penetrations by an overflow pipe that runs to the overflow tank. A small inflow of oil, when required, will make the oil level stable at the level of the overflow runoff.

5.4 Cylindrical Tank Internals

The phototube support structure will consist of an inner shell consisting of 650 aluminum plates on each which will be mounted five phototubes. The plates themselves will be mounted on a series of latitudinal rings supported from the bosses on the tank wall. The volume inside the aluminum plates will form the detector volume, while the outside volume will form the veto shield region. Therefore, the inside surface of the aluminum plates will be painted black, while the outside surface will be painted white. There will be a total of 3900 8-inch detector phototubes, providing 25% coverage of the surface area, and an additional 390 8-inch veto phototubes mounted directly on the tank wall. Each phototube will have one RG58 cable carrying both the high voltage to the phototube and the signal from the phototube. The cables will penetrate the side of the access portal through close fitting holes in the penetration panel, which will be above the oil level.

Light from a laser located in the utility enclosure will be piped along fiber optic cable through an access portal penetration to four 10 cm diameter glass bulbs that are located at various positions in the detector volume of the tank. The bulbs will be filled with LUDOX and will disperse the laser light isotropically, so that the phototubes can be timed accurately relative to each other. In addition, there will be six small scintillator cubes (each 5 cm on a side) that will be used for tracking cosmic-ray muons.

The tank will be filled with oil through a 3-inch diameter pipe that connects to the bottom of the tank. An overflow pipe in the access portal connects to a storage tank and defines the oil level. Nitrogen gas will be bubbled into the tank at various levels and will help maintain a small nitrogen overpressure in the access portal. The nitrogen will purge oxygen and water from the oil.

5.5 Detector Enclosure

The Support Plant is located above the detector tank but below existing grade and consists of areas for electronics, utilities, and tank access. The utilities area includes a reservoir tank to accommodate the variations in oil volume due to small variations in temperature. It also includes the active plumbing elements necessary for oil and nitrogen circulation and the laser used for phototube calibration. The electronics area includes fast electronics, a data acquisition system, a farm of workstations, and a taping system, while the tank access area contains the phototube preamplifier electronics and will provide for personnel and equipment access to the detector tank. An HVAC system, located in and adjacent to the utilities area, will be provided for the enclosure and detector vault. The main entrance and exit will be near the reservoir tank. The electrical power required for operation of the OscSNS experiment is estimated to be ~ 250 kW. It is necessary to separate the electronics power source from the power used in the utility building for pumps, plumbing, and laser calibration. No water cooling is required.

5.6 Gadolinium-loaded Liquid Scintillator Option

The detection of electron anti-neutrinos via the inverse beta-decay reaction is one of the main signals for OscSNS. To maximize observation of this channel, we will need to dope our mineral oil with a liquid scintillator (LS) that will produce large numbers of photons at these lower energies of a few MeV. Previous neutrino experiments have used butyl-PBD and various organic liquid scintillators as the dopant. We are exploring the use of both dopants for OscSNS.

The antineutrino signal is a delayed coincidence between the prompt positron and the capture of the neutron in an (n, γ) reaction after it has been thermalized in the LS. This delayed coincidence tag serves as a powerful tool to reduce random backgrounds.

The neutron capture can occur on the hydrogen in the organic LS, but the cross section is small at 0.332 barns, and only one γ -ray is emitted with the energy of 2.2 MeV. There are several important advantages that come from adding a metallic ion, such as Gadolinium, Gd, to the LS:

(a) The (n, γ) cross-section for natural Gd is high, 49,000 barns (with major contributions from the following Gd isotopes, Gd-152, 1100 barns, 0.2%; Gd-155, 61,000 barns, 14.9%; Gd-157, 254,000 barns, 15.7%). Because of this high cross section, only a small concentration of Gd, $\sim 0.1 - 0.2\%$ by weight, is needed in the LS.

(b) The neutron-capture reaction by Gd releases a sum of 8-MeV energy in a cascade of 3-4 γ -rays. The higher total energy release of the γ -rays and their enhanced isotropy help to exclude low-energy backgrounds from other sources, such as radioactive decay in the surrounding environment and materials. In addition, the higher energy release of 8 MeV, occurs only in the Gd-loaded region of the detector; thus, its fiducial volume and target mass are better defined.

(c) The time delay for the neutron-capture is also significantly shortened to $\sim 27\mu\text{s}$ in 0.1% Gd, as compared to $\sim 200\mu\text{s}$ in H. This shortened delay time reduces the accidental background rate, by a factor of ~ 7 .

A multi-ton scintillation detector for an antineutrino oscillation experiment must satisfy a number of

stringent requirements:

- The Gd-LS must be chemically stable for the life of the experiment; periods of > 3 years are nominally quoted for today’s liquid scintillator experiments.
- The Gd-LS must be optically transparent, have high light output, and have ultra-low concentrations of radioactive and chemical contaminants. “Chemical stability” means any formation over time of any components in the liquid that will absorb or scatter light, or change the concentration. For example, development of color, or gels, or precipitates, or colloids, or hydrolysis, etc., cannot be tolerated.
- The Gd-LS must also be chemically compatible with the containment vessel; for example, it is known that various organic solvents can attack acrylic plastic.

Several organic scintillation solvents were studied to test their feasibilities for the above-mentioned criteria. 1,2,4-trimethylbenzene (pseudocumene, PC) is a clear, fluorescent LS that has been used in previous neutrino experiments at nuclear reactors, because of its high light yield. However, pseudocumene is also known for low flash point, which imposes extra safety concerns, and high chemical reactivity, which causes the problem of chemical incompatibility with the detector vessel that contains the LS. Phenyl cyclohexane (PCH), a colorless benzene-based liquid, has a lower reactivity, but only half of the light yield compared to PC. Both di-isopropylnaphthalene (DIN) and 1-phenyl-1-xylyl ethane (PXE) have absorption bands in the UV region below 450-nm that are difficult to be removed by conventional purification processes, neither by Al₂O₃ exchange-column nor by vacuum distillation (since they have high boiling points). Linear alkylbenzene, LAB, first identified as a scintillation liquid from the SNO+ R&D, is composed of a linear alkyl chain of 10-13 carbons attached to a benzene ring; it is commercially used primarily for the industrial production of biodegradable synthetic detergents. LAB has a light yield comparable to that of PC and a high flash point, which significantly reduces the safety concerns. These notable characteristics make it suitable for a large-scale neutrino experiment. Current ongoing or proposed experiments for reactor electron anti-neutrinos, Daya Bay and RENO, double-beta decay, SNO+, and solar neutrinos, LENS, unanimously select LAB as their primary scintillation liquid. Similarly, OscSNS will use LAB as the baseline solvent for the Gd-loaded option; which has advantage of stability, high light-yield, and optical transmission over a binary solvent system (i.e. PC or LAB in dodecane or mineral oil).

It is commonly known in the community that the quality of Gd-LS is the key to the success of the LS experiments. There is heightened concern for a new long-duration oscillation experiment such as we propose here. The BNL neutrino and nuclear chemistry group has been involved in R&D of chemical techniques for synthesizing metal-loaded organic liquid scintillators since 2000 and is currently a member of several liquid scintillator experiments: Daya Bay, SNO+ and LENS. A highly stable 0.1% Gd-LS with attenuation length of ~ 20 m and $\sim 10,000$ optical photons/MeV has been developed by the BNL group for the reactor antineutrino experiments. Indeed, Daya Bay has published its first observation of non-zero θ_{13} in 2012, based on the successful detection of the IBD reaction by Gd-loaded liquid scintillator.

Even though the synthesis procedures already give satisfactory, consistent results and has been demonstrated by modern reactor experiments, once the Gd-loaded option is selected, we intend to further perfect the methods of synthesis and purification (both chemical and radioactive) to advance their reliability and reproducibility, especially to further enhance the optical transmission of Gd-LS to better than 25m for large LS detectors ($> \text{kton}$) used for neutrino oscillation experiments. A list of the tasks that we will undertake for OscSNS includes:

- (1) Continue the R&D of Gd-loaded in singular system (LAB).
- (2) Start the R&D of Gd-loaded in binary system (LAB in dodecane or mineral oil).
- (3) Design the mass-production scheme and develop the QA/QC protocols for raw material and liquid quality control.
- (4) Test a broad selection of candidate organic scintillators, in addition to LAB and their mixtures of any inert solvents.
- (5) Study the chemical compatibility of these organic LS with the materials that will be used to construct the OscSNS detector vessel.
- (6) Develop methods to remove and assay radioactive contaminants, mainly from the naturally occurring U-238 and Th-232 decay chains.

5.7 Electronics and Data Acquisition

The phototubes, preamplifier boards, and digitization electronics for OscSNS will be similar to the system used for LSND and MiniBooNE. This system has a clock rate of 10MHz, sufficient memory available for 200 μ s of data before being overwritten, and is described in detail elsewhere [12]. Improved electronics will have a clock rate of 200MHz. A precursor signal from the accelerator will be used to record data for a period of about 20 μ s around each 695 ns beam spill. In addition, there will be other triggers used for calibration.

The OscSNS data acquisition system will be based on the LSND/MiniBooNE system. The 14 crates of electronics will be read out by monoboards located in each crate, and the data will be sent to the multi-processor computer that will build and reconstruct the events in real time. The reconstructed events will then be written to disk and logged to tape. A high-speed link will connect the control room to the multi-processor computer, so that the experiment can be monitored and analyzed in real time from the OscSNS control room.

5.8 Calibration

The accurate measurement of event interactions and neutrino oscillations requires a well-calibrated detector in the range from 1 MeV to 50 MeV.

The calibration system is designed to (1) provide information on the PMT response that is needed as input for the event reconstruction and particle identification calculations, (2) calibrate the position, energy and direction determination of the reconstruction program using stopping cosmic ray muons and Michel electrons from muon decay (end-point energy of 52.8 MeV) and (3) measure the attenuation of light by the oil in the detector tank.

The cosmic-ray muons can be reconstructed by a high-resolution muon tracker mounted above the detector tank, and scintillator cubes inside the detector. The tracker is made of scintillator strips and will also help with the rejection of cosmic-ray background and improve the efficiency of the veto system. The muon tracker will give the direction of cosmic-ray muons while the cubes will give a precise position measurement of

stopping muons and decay electrons.

In addition to the cosmic-ray calibration, radioactive calibration sources producing both gamma-rays and neutrons are desirable. A partial list of potential sources are:

- ^{16}N source: [$^{16}\text{O}(n, p)^{16}\text{N}^*$] producing a β -tagged 6.1 MeV gamma-ray.
- ^8Li source: electron energy spectrum up to 15 MeV.
- pT source: [$^3(p, \gamma)^4\text{He}$] producing a 19.8 MeV gamma-ray.
- ^{252}Cf source: producing fission neutrons.

A flexible deployment system similar to that of SNO is envisioned, whereby the above sources can be moved to any position within the detector volume [13]. This will allow a precise determination of optical properties and detector response throughout the entire detector volume. This is crucial for the precision neutrino measurements envisioned for OscSNS.

The laser calibration system will provide short pulses of light from a tunable dye laser to 4 flasks at various locations in the detector. The system is very similar to the system used successfully in LSND and MiniBooNE. It is used to determine phototube time-offsets and gains and to determine time-slewing corrections.

The oil monitoring system will measure attenuation of light as a function of wavelength in the detector.

Chapter 6

SNS Neutrino Flux Simulation

The OscSNS experiment uses Geant4 [14] to simulate the interaction of the proton beam with the liquid mercury target. Approximately 17% of the incident protons interact to produce a charged pion (π^+ , π^-). These charged pions are brought to rest on a short time scale (< 3 ns), due to their relatively low energy at creation (~ 200 MeV), and to the high stopping power of the target material.

Over 99% of the produced π^+ decay at rest. The pion has spin 0, which causes its decay products, μ^+ and ν_μ , to be emitted isotropically. The subsequent μ^+ decay occurs within 0.2 g/cm² of the point at which the π^+ stopped. The $\bar{\nu}_\mu$ and ν_e fluxes are also isotropic.

The bulk of the π^- produced are absorbed by the target before they are able to decay. Less than 1% of the produced π^- decay, all of which decay in flight.

The majority of the pions and muons decay in the immediate vicinity of their production point. A neutron spallation facility, therefore, produces an extremely intense, approximately point-like, source of neutrinos for nuclear and particle physics studies.

The complete simulation chain consists of the following stages:

- Simulate p+Hg interaction
 - This interaction produces the mesons (π , μ), and allows the particles to decay to produce the full neutrino flux coming from the SNS. We then select only those neutrinos whose direction is 150 degrees, with respect to the proton direction.
- The generated fluxes are used to produce the interactions inside detector volume. These interactions produce outgoing charged leptons.
- The resulting leptons are fed into another Geant4 package that models the OscSNS detector. The photons from Cerenkov radiation and scintillation produced by the leptons are recorded in the PMTs. Coordinates of the activated PMTs, together with the number of photons and timing information, are saved as histograms. This information is then used as input for the particle identification and reconstruction algorithms.

6.1 Generation of Neutrino Fluxes

A preliminary Monte Carlo simulation for the interaction of the proton beam with the mercury target was done with Geant4 [14]. This software package is currently the most widespread simulation tool in the nuclear and high energy physics community. This is due to its versatility and preciseness in the description of incident particle beams, involved physics models, and geometry visualization. Geant4 is open source code that is maintained by a core group of personnel, and as such is constantly improving.

There are four major components to our neutrino flux simulation: generation of primary particles, simulation of the target hall geometry, physics processes available to the incident protons and produced mesons, and particle counters and histograms.

6.1.1 Generation of Primary Particles

Geant4 provides a convenient tool for configuration of the incident beam (General Particle Source [15]). The 1 GeV proton beam was randomly distributed within a rectangle with 200 mm x 70 mm cross-sectional area (similar to the SNS beam spot size), and was perpendicularly incident on the target surface. Beam timing information (695 ns pulse duration with 60 Hz repetition rate) was also included to better approximate the experimental conditions.

6.1.2 Description of Geometry

The SNS target hall consists of thousands of various parts, many of them very complex shapes. Thus, for the preliminary simulation, a simplified target hall geometry was chosen. The target hall model consists of the 400 mm x 104 mm x 500 mm liquid mercury target, surrounded in stainless steel casing. We have also included major bulk parts surrounding the target area, that are composed primarily of steel and concrete. The center of the detector is placed at ~ 60 m from the interaction point, at an angle of ~ 150 degrees from the proton beam direction. Fig. 6.1 shows a schematic drawing of the detector location in relation to the SNS target hall.

6.1.3 Description of Physics Processes

In Geant4 terms, a physics list is a compilation of processes or interactions that particles are permitted to engage in, for varying energy ranges. Creating an acceptable physics list for a simulation is a challenging task (see e.g. [16]). The Geant4 collaboration provides a collection of pre-compiled physics lists for various applications. For most physics applications, these physics lists are good only for a first order rate estimate. Final experimental simulations require modifications to these pre-compiled lists. Our rate estimates are based on the QGSP_BERT list. It uses the quark-gluon string model for high energies (> 20 GeV), low energy parameterized for medium energies ($10 < E \leq 20$ GeV), and Bertini-style cascade for low energies (≤ 10 GeV).

This list was validated by calculating the lifetime of negative muons in various materials. For better event statistics, a beam of 100 MeV μ^- was generated in the center of the target box, with an isotropic angular

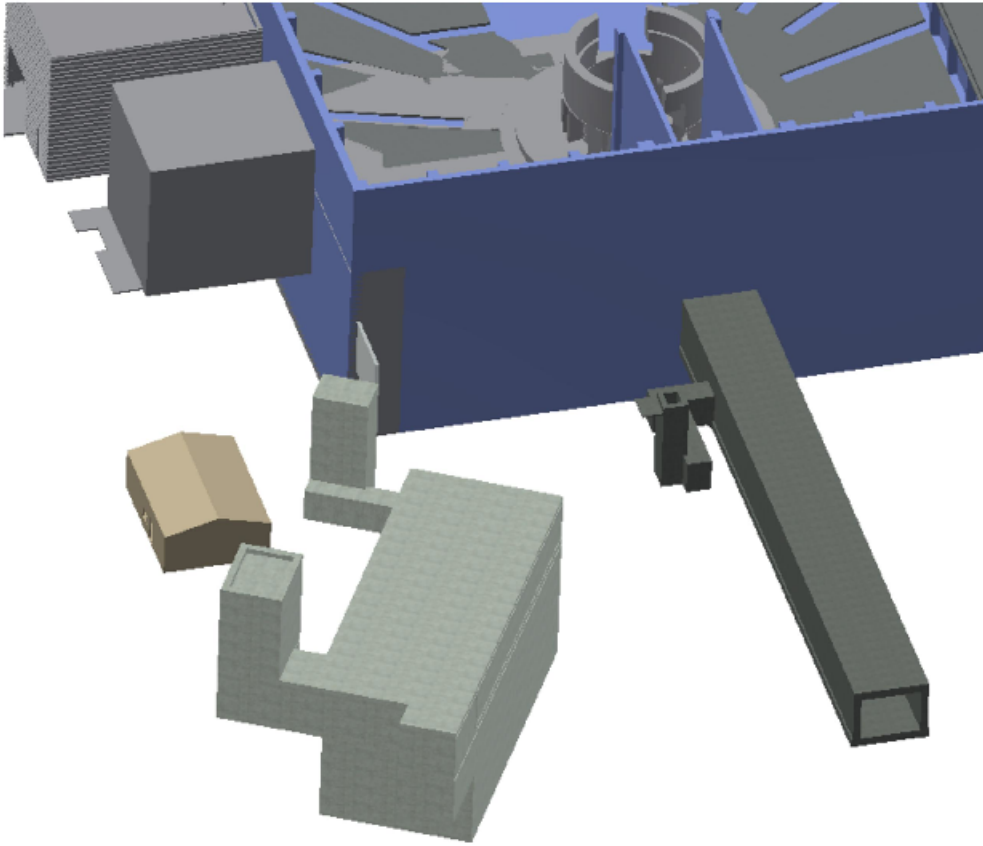


Figure 6.1: A schematic drawing of the detector location in relation to the SNS target hall.

Material	Lifetime, ns (experiment)	Lifetime, ns (calculation with QGSP_BERT)
Be	2162.1 ± 2.0	2161.0
Fe	206.0 ± 1.0	205.9
Hg	76.2 ± 1.5	72.3

Table 6.1: Lifetime values for negative muons calculated with Geant4, compared to experimental data. Data is taken from [17]

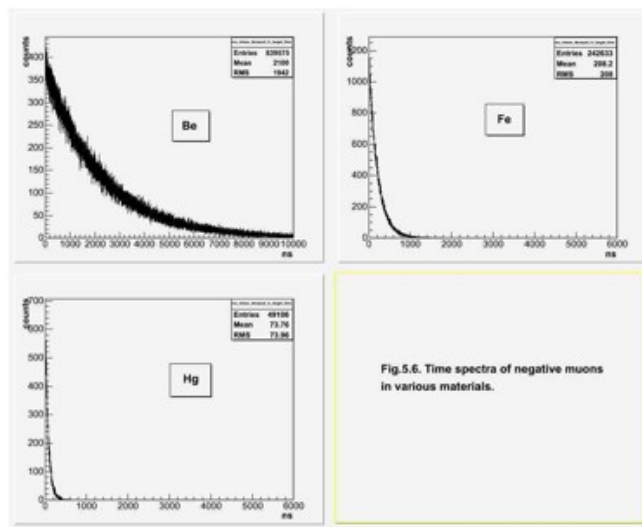


Figure 6.2: Time spectra of negative muons in various materials.

distribution. This list produces good agreement between the experimental data and the simulation results (see Table 6.1). The corresponding time spectra are shown in Figure 6.2. The lifetime values were deduced by fitting the time histograms with an exponent.

Using QGSP_BERT, the yields (number of produced particles per proton-on-target) are 0.116 for π^+ and 0.059 for π^- . This results in the following yield values for various neutrino flavors: 0.09 for ν_e , ν_μ , $\bar{\nu}_\mu$, and $1.15e^{-4}$ for $\bar{\nu}_e$. We plan to further improve the Geant4 physics list for final rate estimates.

6.1.4 Particle Counters and Histograms.

Energy and time distributions of the charged pions, muons, and the corresponding neutrinos were written into ROOT [18] histograms. The flux of neutrinos originating from the SNS target area (pion and muon decay, muon capture) are shown in the Figure 6.3. The feature in the ν_μ spectra around 90 MeV comes from a Geant4 process, muMinusCaptureAtRest. This process is built in to the Geant4 physics lists, and is model dependent. There is no experimental data to guide the prediction of these interactions, and thus it has large uncertainties associated with it. Future flux estimates will carefully study and consider the inclusion

of this process into the final prediction. The corresponding time distributions of these neutrinos are found in Figure 6.4.

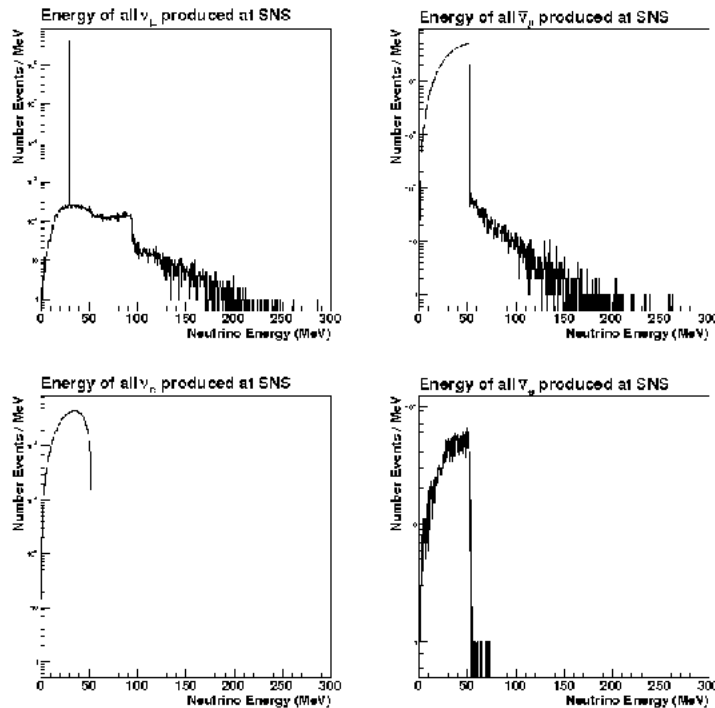


Figure 6.3: Energy spectra of neutrinos produced from the decay of pions and muons at the SNS. From left to right, top: ν_μ , $\bar{\nu}_\mu$; bottom: ν_e , $\bar{\nu}_e$. Rates are for 50M protons on target. The prominent feature in the ν_μ spectra around 90 MeV comes from the muMinusCaptureAtRest process in Geant4.

Almost all negative muons and pions are captured in the target prior to decaying. The small percent of negative mesons that decay in flight are boosted in the direction of the proton beam. Neutrinos originating from decays in flight are primarily emitted in the forward direction (see Figure 6.5). We have chosen to place our detector in the backward direction, relative to the proton beam, to reduce this background to a negligible level. Almost no neutrinos from particles decaying in flight are seen in the detector.

The neutrinos produced from the decays at rest in the target are distributed isotropically. This may be seen by comparing the ratios:

$$\frac{\text{AREA SUBTENDED BY DETECTOR}}{4\pi R^2} \quad (6.1)$$

and

$$\frac{\text{NUMER OF } \nu \text{ IN DETECTOR}}{\text{TOTAL NUMBER OF } \nu}, \quad (6.2)$$

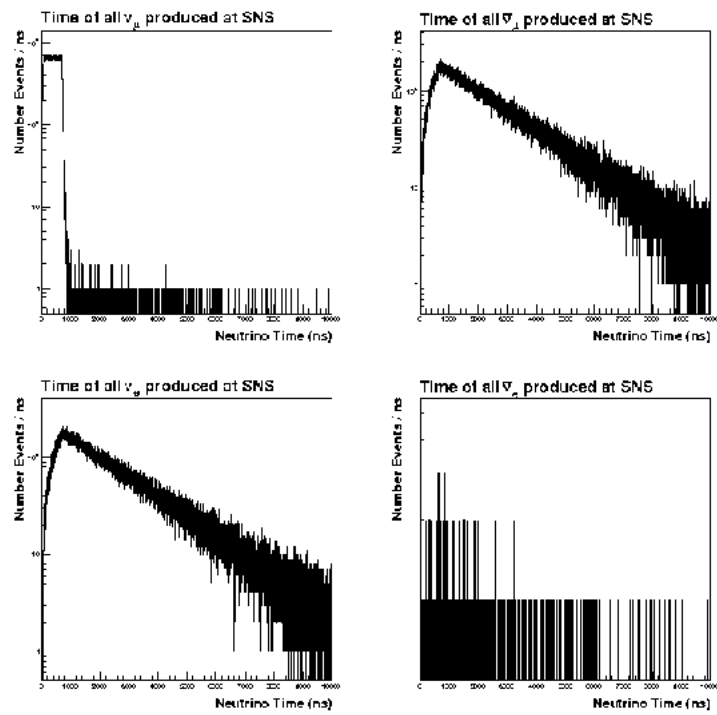


Figure 6.4: Time spectra corresponding to Figure 6.3. From left to right, top: ν_μ , $\bar{\nu}_\mu$; bottom: ν_e , $\bar{\nu}_e$. Rates are for 50M protons on target.

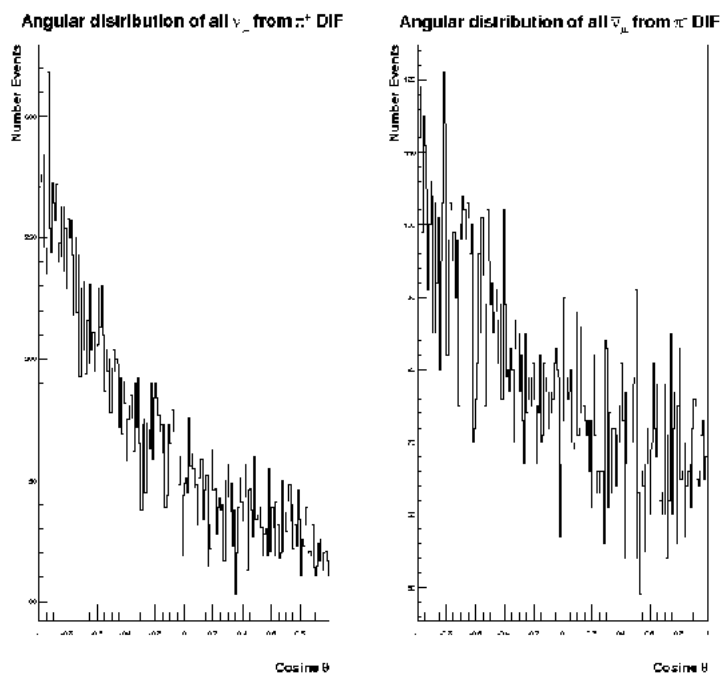


Figure 6.5: Angular distributions for muon neutrinos (left) and anti-neutrinos (right), from all decays in flight of positive and negative pions, respectively. The angle is taken between the emitted neutrino direction and the direction to the detector. Rates are for 50M protons on target.

where R is the distance from the target to the detector cylinder. For 5×10^7 incident protons, these ratios for muon neutrinos are 0.0025 and 0.002548, respectively.

It should be stressed that the $\bar{\nu}_e$ production is a factor of 10^{-3} to 10^{-4} lower than the other neutrino species. A large reduction in the $\bar{\nu}_e$ flux is due to the strong absorption of π^- and μ^- in the SNS mercury target. Decay of μ^- is the primary source of $\bar{\nu}_e$; additional $\bar{\nu}_e$ are produced via the decay of $\pi^- \rightarrow e^- \bar{\nu}_e$, with a branching ratio of $\sim 1.2 \times 10^{-4}$. Additional reductions to the $\bar{\nu}_e$ background will result from the use of the time structure in the SNS proton beam. The time spectrum of $\bar{\nu}_e$ from the decay at rest of μ^- consists of two basic components: (1) an exponential decay in low- Z materials, such as Be and Al, dominated by the 2.2 μs muon mean life, and (2) the much faster exponential decay in high- Z materials mercury, lead, and iron characterized by a fast absorption rate. Events are separated into two time groups, above and below 1000 ns from the start of the proton pulse. A time-cut at 1000 ns will eliminate the $\bar{\nu}_e$ background from μ^- decay in mercury and iron, thereby reducing the background by a factor of two. More importantly, comparing the rates of appearance of $\bar{\nu}_e$ before and after the 1000 ns cut provides for the first time an opportunity to experimentally evaluate the $\bar{\nu}_e$ background.

6.2 Simulation of Neutrino Interactions

At its present development stage, Geant4 does not simulate neutrino interactions. Therefore, a separate program was written in Fortran77 for that purpose. The neutrino energy spectra histograms produced by Geant4 are used as inputs to this program.

The Fortran code calculates cross-sections for quasi-elastic neutrino scattering with the nucleon bound inside a nucleus, and quasi-elastic neutrino-nucleus scattering using the Fermi gas model. The code can also be easily modified to calculate other reactions of interest.

The output file contains the coordinates of the outgoing lepton vertex, its energy, differential cross-section, and direction (as $\cos\theta$ and ϕ). Since the cross-section values are relative, the events have to be weighted. One way to achieve this is as follows. For a given number of events, the maximum value of the cross-section is determined. Then, for each individual event, the ratio of its cross-section to the maximum value is calculated and is compared to the random number generated in the (0,1) interval. The event is passed to the output file if the ratio is greater than the random number, and is neglected otherwise. The resulting file is supplied to another Geant4 package to simulate the propagation of produced leptons inside the detector.

Chapter 7

OscSNS Detector Simulation

A Monte Carlo simulation was written to simulate events in the detector using GEANT4 [14]. The simulated detector consists of a cylindrical tank filled with mineral oil which has been laced with butyl-PBD (butyl-phenyl-biphenyl-oxydiazole) scintillator at a concentration of 0.031 g/l. The inner region of the detector has a radius of 3.65 m, and is surrounded by 3900 photomultiplier tubes. The photomultiplier tubes were modeled as hemispheres of radius 10.1 cm containing photocathodes of cross-sectional radius 9.5 cm. The photocathode surface was located 15 cm inside the central tank wall. This arrangement yields a mean photocathode coverage of 25%.

Standard Geant4 packages were used to simulate particle interactions within the detector. Parameters used to simulate the optical model were taken from studies conducted by previous experiments. In particular, the values for the refractive index and absorption length spectra of the mineral oil were determined using values measured by MiniBooNE [19]. The actual detector will also contain a small concentration of butyl-PBD. The MiniBooNE values for these quantities are adequate for preliminary studies.

The parameters used to simulate scintillation light were taken from studies conducted by the LSND collaboration at the Area A test channel of the Los Alamos Meson Physics Facility (LAMPF) [20]. Scintillation light typically has both fast and slow components. The ratio of slow to fast scintillation light produced by an ionizing particle depends upon the dE/dx of the particle, as the amount of fast scintillation light produced saturates at higher dE/dx as described by Birks' law [21]. The LSND study measured the properties of Cerenkov and scintillation light for both positrons and protons. While the scintillation time constants should be the same for all types of charged particles, the LSND measurements of the isotropic time constants differed for positrons and protons. This difference was due to Cerenkov light produced by the positrons being absorbed and re-emitted isotropically, thus contaminating the isotropic light generated by pure scintillation light. For the OscSNS optical model we are taking the scintillation time constants to be those measured for protons, which were produced below the Cerenkov threshold and should therefore have no such contamination in their measured isotropic light.

The LSND study also measured the relative amounts of slow and fast scintillation light produced by both particle types, the values of which are also used in the simulation. These values are listed in table 7.1. The scintillation yield was set arbitrarily high so that studies could be conducted to determine the optimum

scintillation light yield using the reconstruction code.

Fast time constant	2.99	± 0.06 ns
Slow time constant	34.34	± 1.51 ns

	Fast Component (%)	Slow Component (%)
e^+/e^-	56.5 ± 0.9	42.5 ± 0.9
p	43.1 ± 0.7	56.9 ± 0.7

Table 7.1: Scintillation time constants, and relative yields of fast and slow scintillation light used in simulation. Values are taken from [20], see text for details.

Chapter 8

Event Reconstruction and Particle Identification

The event reconstruction in OscSNS is performed using a maximum likelihood algorithm which is based on the recorded charge and time information of all 3900 PMTs in the inner detector, regardless of whether they are hit or not. For an event characterized by a set of parameters α , such as event vertex, time, energy, etc., the likelihood for an observed set of PMT measurements is given by

$$\mathcal{L}_{event} = \prod_{i=nohit} \left[1 - P_{hit}(\alpha) \right] \times \prod_{i=hit} P_{hit}(\alpha) f_q(q_i; \alpha) f_t(t_i; \alpha),$$

where:

- (i) $P_{hit}(\alpha)$ is the probability of the i th PMT to be hit given the event parameters α ,
- (ii) (q_i, t_i) are the measured charge and time on the i th hit PMT,
- (iii) $f_q(q_i; \alpha)$ is the probability distribution function (PDF) for the measured charge on the i th hit PMT given the event parameters α , evaluated at the measured value q_i , and
- (iv) $f_t(q_i; \alpha)$ is the PDF for the measured time on the i th hit PMT given the event parameters α , evaluated at the measured value t_i .

Generally, it is more convenient to work with the negative logarithm of the event likelihood, and since the charge- and time-related portions of the likelihood decouple naturally, we define

$$F(\alpha) \equiv -\ln \mathcal{L}_{event}(\alpha) \equiv F_q(\alpha) + F_t(\alpha),$$

where

$$\begin{aligned} F_q(\alpha) &= - \sum_{i=nohit} \ln \left[1 - P_{hit}(\alpha) \right] - \sum_{i=hit} \ln \left[P_{hit}(\alpha) f_q(q_i; \alpha) \right], \\ F_t(\alpha) &= - \sum_{i=hit} \ln \left[f_t(t_i; \alpha) \right]. \end{aligned}$$

For brevity, we shall refer to F_q and F_t as the charge and time likelihoods, respectively, although strictly speaking they are the negative logarithms of the likelihoods.

Both charge and time PDFs which enter the calculation of the likelihoods can be obtained both from MC simulations and self-consistently from the data (either calibration or cosmic-ray induced). Furthermore, assuming that the PMT discriminator level is set low enough, the hit probability for any given PMT can be assumed to be simply $P_{hit}(\boldsymbol{\alpha}) = 1 - \exp(-\mu)$, where μ is the amount of predicted charge at the PMT given the set of event parameters $\boldsymbol{\alpha}$. The exact form of the PMT hit probability function can be measured *in situ* from low-intensity laser calibration data.

For electrons, the event is fully characterized by a set of seven parameters: the event vertex, time, direction and energy,

$$\boldsymbol{\alpha}_e = (x_0, y_0, z_0, t_0, \varphi, \theta, E_e),$$

where (θ, ϕ) give the event direction in the detector's coordinate system, whereas a neutron is fully characterized by only five parameters, namely the event 4-vertex and the visible energy:

$$\boldsymbol{\alpha}_n = (x_0, y_0, z_0, t_0, E_n).$$

Each event is reconstructed under two different hypotheses, namely under the electron model, which yields an event likelihood \mathcal{L}_e , and under the neutron model, which yields an event likelihood \mathcal{L}_n . The ratio of these two likelihoods, or equivalently, the difference in the negative log-likelihoods,

$$\ln \frac{\mathcal{L}_e}{\mathcal{L}_n} = F_n - F_e$$

serves as particle identification.

Fig. 8.1 shows the separation of electrons and protons that was achieved with the LSND experiment [2]. The parameter χ_L depended on three quantities: the fit to the Cerenkov cone, the position and angle fit, and the fraction of hit PMTs that had times more than 10 ns later than the fitted times. Electron events could clearly be distinguished from proton and neutron events.

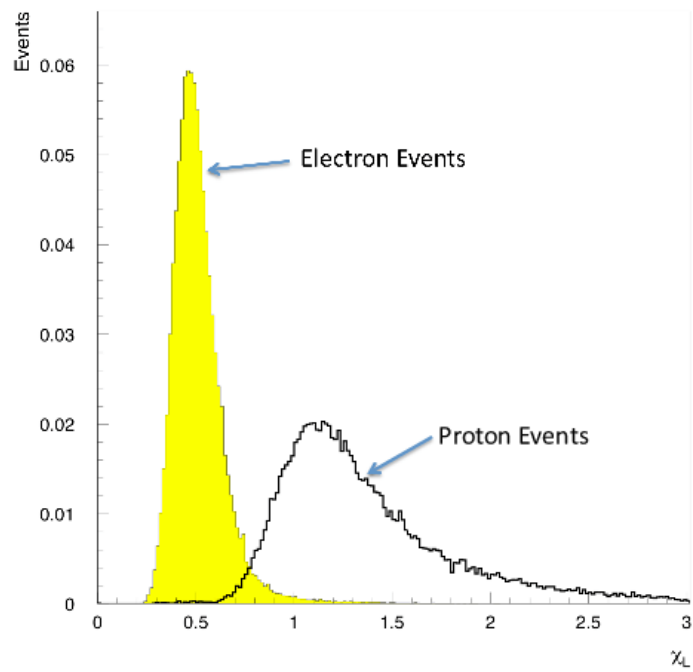


Figure 8.1: The separation of electrons and protons that was achieved with the LSND experiment [2].

Chapter 9

Event Rates and Sensitivity Predictions

The OscSNS experiment offers a complete physics program encompassing beyond the Standard Model searches as well as precision cross section measurements. The following chapter details the event rate expectations for each of the physics goals, and provides sensitivity predictions for the oscillation searches. These predictions are based on neutrino backgrounds only. In addition, we expect a small contribution from cosmic-ray background, which is assumed to be negligible in this preliminary study.

The number of expected neutrino events of a given interaction type is

$$\Phi (\nu/year/cm^2) \cdot \sigma (cm^2) \cdot N_{targets}, \quad (9.1)$$

where Φ is the neutrino flux seen at the detector, σ is the cross section for the interaction, and $N_{targets}$ is the number of targets in the volume of the detector. Carbon is the target material for the sterile neutrino (disappearance) oscillation search, carbon and free protons are the targets for the appearance oscillation searches, and carbon only is the target for the ν_e C \rightarrow e⁻ N cross section measurement. Electrons are the target material for the elastic scattering cross section measurement.

9.1 Cross Section and Target Information

The following list describes the complete suite of measurements that OscSNS will be performing:

- Neutrino-electron elastic scattering used for cross section measurements:

$$\begin{aligned} & - \nu_e e^- \rightarrow \nu_e e^- \\ & - \nu_\mu e^- \rightarrow \nu_\mu e^- \\ & - \bar{\nu}_\mu e^- \rightarrow \bar{\nu}_\mu e^- \end{aligned}$$

- Neutral current (NC) interaction channels are used to search for oscillations into sterile neutrinos. These analyses look for a deficit (disappearance) of events over what is expected based on a non-oscillation hypothesis. The relevant processes are:

$$\begin{aligned}
& - \nu \ ^{12}\text{C} \rightarrow \nu \ ^{12}\text{C}^* \ (\nu_\mu \text{ disappearance, all disappearance}) \\
& - \bar{\nu} \ ^{12}\text{C} \rightarrow \bar{\nu} \ ^{12}\text{C}^* \ (\text{all disappearance})
\end{aligned}$$

- Charged current (CC) interaction channel are used to search for oscillations into sterile neutrinos. This analysis looks for a deficit (disappearance) of events over what is expected based on a non-oscillation hypothesis. The relevant process is:

$$- \nu_e \ ^{12}\text{C} \rightarrow e^- \ ^{12}\text{N}_{gs} \ (\nu_e \text{ disappearance})$$

- Charged current (CC) interaction channels are employed in the appearance oscillation searches. These analyses look for an excess of events over those coming from neutrinos inherent, or intrinsic, to the beam (i.e. background events).

$$\begin{aligned}
& - \bar{\nu}_e \ ^{12}\text{C} \rightarrow e^+ \ ^{12}\text{B} \ (\bar{\nu}_e \text{ appearance}) \\
& - \bar{\nu}_e \ p \rightarrow e^+ \ n \ (\bar{\nu}_e \text{ appearance}) \\
& - \nu_e \ ^{12}\text{C} \rightarrow e^- \ ^{12}\text{N}_{gs} \ (\text{mono-energetic } \nu_e \text{ appearance})
\end{aligned}$$

The cross section predictions used in the event rate estimates come from References [22, 23, 24], and are provided as a function of incident neutrino energy. Input cross section histograms are shown in Figure 9.1.

The density of mineral oil (CH_2) is 0.86 grams/cm³. The target mass is the density times the fiducial volume of the detector (523 m³) or 450 tonnes. The total mass divided by the mass of CH_2 ($2.32 \cdot 10^{-23}$ grams) gives the number of CH_2 molecules in the detector. For the above interactions on carbon, the number of molecules is the same as the number of ¹²C targets. The total number of CH_2 targets is then

$$\frac{0.86 \text{ g/cm}^3 \cdot 523 \text{m}^3}{2.32 \cdot 10^{-23} \text{ g}}, \tag{9.2}$$

or $1.94 \cdot 10^{31}$ ¹²C targets. The total number of free proton targets (for the appearance search) is 2 times the number of carbon targets, or $3.9 \cdot 10^{31}$ targets. The total number of electron targets for the neutrino-electron scattering cross sections is 8 times the number of CH_2 molecules or $15.5 \cdot 10^{31}$ ¹² electron targets.

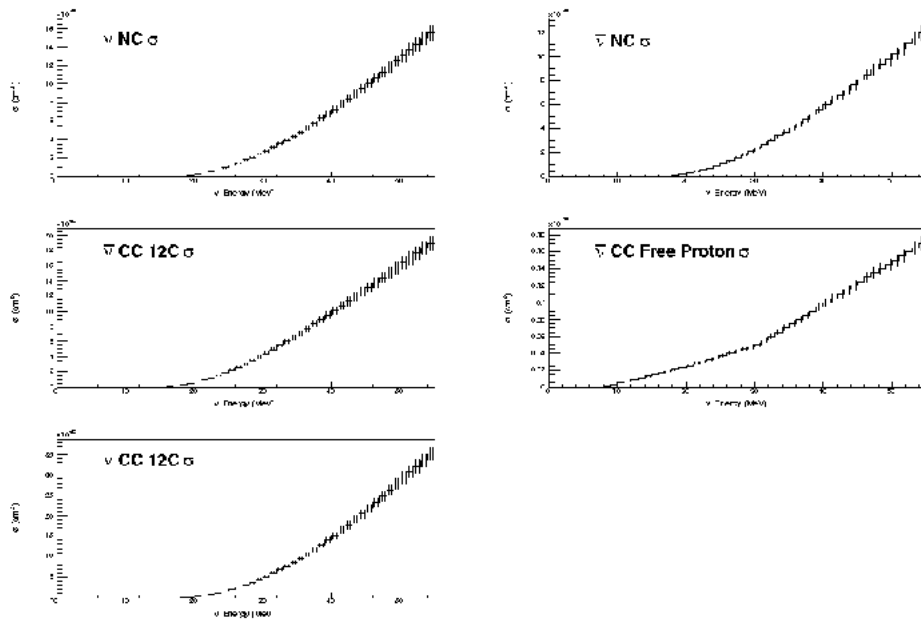


Figure 9.1: Input cross sections as a function of incident neutrino energy. Cross section plots include a 5% uncertainty. From left to right, top: ν $^{12}\text{C} \rightarrow ^{12}\text{C}^*$, $\bar{\nu}$ $^{12}\text{C} \rightarrow ^{12}\text{C}^*$; middle: $\bar{\nu}_e$ $^{12}\text{C} \rightarrow e^+ ^{12}\text{B}$, $\bar{\nu}_e$ $p \rightarrow e^+ n$; bottom: ν_e $^{12}\text{C} \rightarrow e^- ^{12}\text{N}$.

9.2 Total Expected Flux

The flux estimates come from a Geant4 simulation of the proton-mercury interaction, described in more detail in Chapter 6. The flux rates are for a detector located 60 meters away from the interaction (creation of neutrinos) point, ~ 150 degrees in the backward direction from the proton beam, and are for 50M simulated protons on target (POT), resulting in the following number of neutrinos passing through the detector: $\nu_\mu = 11289$, $\nu_e = 11224$, $\bar{\nu}_\mu = 11357$, $\bar{\nu}_e = 15$ (See Figure 9.2). The majority of these neutrinos come from particles decaying at rest (DAR). Only 0.23% of the neutrino beam seen by the detector originate from mesons decaying in flight (DIF).

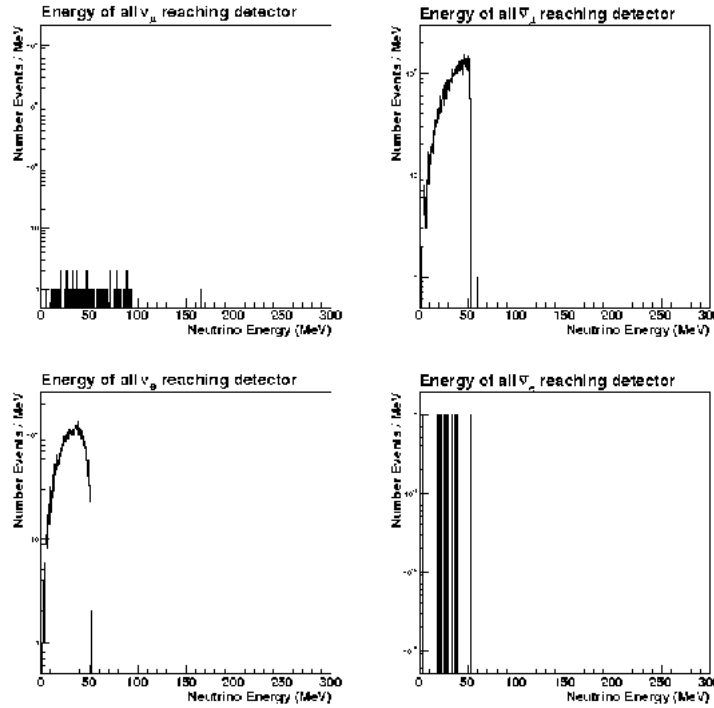


Figure 9.2: Input flux as a function of incident neutrino energy, for neutrinos reaching the detector. These plots include neutrinos from DAR and DIF. From left to right, top: ν_μ , $\bar{\nu}_\mu$; bottom: ν_e , $\bar{\nu}_e$. Rates are for 50M simulated protons on target.

The neutrino flux per year is found by assuming $8.7 \cdot 10^{15}$ POT/second from the SNS (for ~ 1.4 MW beam power), or $2.74 \cdot 10^{23}$ POT/year. Dividing this by 50M results in a conversion factor of $5.5 \cdot 10^{15}$ POT/year. The expected neutrino fluxes are:

- $\nu_\mu = 2.48 \pm 0.02 \cdot 10^{22} \nu/\text{year}$
- $\nu_e = 2.46 \pm 0.02 \cdot 10^{22} \nu/\text{year}$

- $\bar{\nu}_\mu = 2.50 \pm 0.02 \cdot 10^{22} \nu/\text{year}$
- $\bar{\nu}_e = 3.30 \pm 0.85 \cdot 10^{19} \nu/\text{year},$

where errors are statistical. The flux per cm^2 is

$$\frac{\text{neutrino flux}}{4\pi \cdot (6000 \text{ cm})^2}, \quad (9.3)$$

which results in the following rates:

- $\nu_\mu = 5.48 \pm 0.05 \cdot 10^{13} \nu/\text{year}/\text{cm}^2$
- $\nu_e = 5.45 \pm 0.05 \cdot 10^{13} \nu/\text{year}/\text{cm}^2$
- $\bar{\nu}_\mu = 5.51 \pm 0.05 \cdot 10^{13} \nu/\text{year}/\text{cm}^2$
- $\bar{\nu}_e = 7.28 \pm 1.88 \cdot 10^{10} \nu/\text{year}/\text{cm}^2$

The total neutrino flux at the detector is $\sim 1.64 \cdot 10^{14} \nu/\text{year}/\text{cm}^2$. The flux numbers quoted above are the final fluxes expected, integrated over the entire energy spectrum for each neutrino type.

9.3 Disappearance Sensitivity

For the disappearance sensitivity, we find the number of non-oscillated events by multiplying the intrinsic neutrino flux by the 2-neutrino oscillation probability:

$$P = 1 - \sin^2 2\theta \sin^2\left(\frac{1.27\Delta m^2 L}{E}\right) \quad (9.4)$$

In the above equation, L is the distance traveled by the neutrino ($50 < L < 70$ m) and E is the neutrino energy ($E = 30$ MeV for ν_μ disappearance and approximately $30 < E < 52.8$ MeV for ν_e disappearance). Best fits to the world data [25, 26, 27, 7] predict values of $\sin^2 2\theta$ to be $\sim 10 - 15\%$ for both ν_μ and ν_e disappearance.

9.4 Appearance Sensitivity : $\bar{\nu}_\mu \rightarrow \bar{\nu}_e, \nu_\mu \rightarrow \nu_e$

For the appearance sensitivity we start with the $\bar{\nu}_\mu(\nu_\mu)$ neutrino flux, and assume 100% transmutation. This number of transmuted $\bar{\nu}_e(\nu_e)$ is multiplied by the 2-neutrino oscillation probability:

$$P = \sin^2 2\theta \sin^2\left(\frac{1.27\Delta m^2 L}{E}\right) \quad (9.5)$$

Best fits to the world data [25, 26, 27, 7] predict values of $\sin^2 2\theta$ to be $\sim 0.3 - 0.5\%$. (Note that $\sin^2 2\theta$ is different for appearance and disappearance oscillations.) The oscillated event spectrum is added to the intrinsic $\bar{\nu}_e(\nu_e)$ spectrum, to produce the final spectrum of observed events.

9.5 Event Rates and Background Estimates

Event rate estimates are based on fluxes seen by the full volume of the detector. However, final estimates need to scale rates to the expected fiducial volume (6 m diameter by 18.5 m long) and to include reductions due to detector efficiency (50%) and beam-on efficiency (50%).

Errors on the rate estimates comprise statistical errors and a 5% systematic error on the neutrino fluxes and cross sections.

9.5.1 ν_μ Disappearance Analysis

For the $\nu_\mu \rightarrow \nu_{sterile}$ search, we look for a deficit in the expected number of neutral current ν_μ $^{12}C \rightarrow \nu_\mu$ $^{12}C^*$ events. The total number of these interactions per year, in the absence of oscillations to a sterile neutrino, for a detector at 60 meters from the interaction point, is

$$5.48 \cdot 10^{13} \nu / \text{year} / \text{cm}^2 \cdot \sigma_{\nu_\mu} \ ^{12}C \rightarrow \nu_\mu \ ^{12}C^* \cdot 1.94 \cdot 10^{31} \ ^{12}C \ \text{targets}, \quad (9.6)$$

or 2977 events per year, where $\sigma_{\nu_\mu} \ ^{12}C \rightarrow \nu_\mu \ ^{12}C^* = 2.8 \times 10^{-42} \text{ cm}^2$ [23]. After reductions due to detector efficiency (50%) and beam-on efficiency (50%) this becomes **745 \pm 42 expected events per year**.

If we perform the search using the entire neutrino flux from ν_μ , ν_e , and $\bar{\nu}_\mu$, where $\sigma_{\nu^{12}C \rightarrow \nu^{12}C^*} = 13.3 \times 10^{-42} \text{ cm}^2$ [23], we expect 14,140 events per year, in the absence of oscillations. This reduces to **3535 \pm 182 events per year** after reductions due to detector efficiency (50%) and beam-on efficiency (50%).

The estimated background under the 15.11 MeV γ peak is approximately 30%, which is obtained from the KARMEN experiment [10] after subtracting the fast neutron background. This should be much lower for OscSNS due to the increased amount of passive shielding between the beam dump and the detector. Fig. 9.3 shows the KARMEN measurement of ν_μ $^{12}C \rightarrow \nu_\mu$ $^{12}C^*$, where the shaded region corresponds to the fast neutron background and the hatched region corresponds to the neutrino and cosmic ray backgrounds. The right plot shows the background subtracted signal. Sensitivity curves in $\sin^2 2\theta$ - Δm^2 space are shown in Figure 9.4 and Figure 9.5 for ν_μ and the complete neutrino flux, respectively. Sensitivity curves are given for two calendar years and for six calendar years of running.

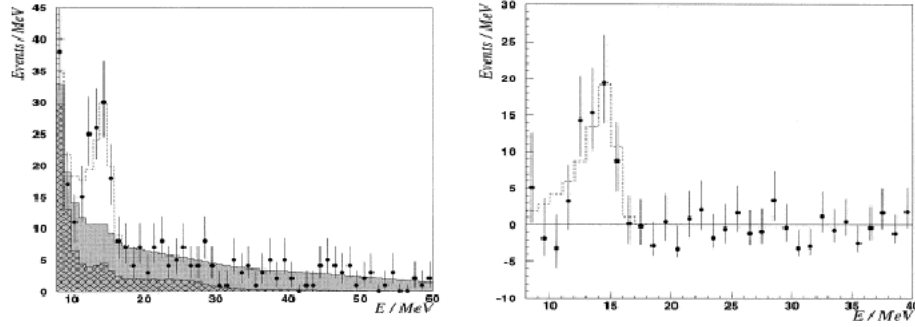


Figure 9.3: The KARMEN measurement of $\nu_\mu \ ^{12}\text{C} \rightarrow \nu_\mu \ ^{12}\text{C}^*$, where the shaded region corresponds to the fast neutron background and the hatched region corresponds to the neutrino and cosmic ray backgrounds. The right plot shows the background subtracted signal.

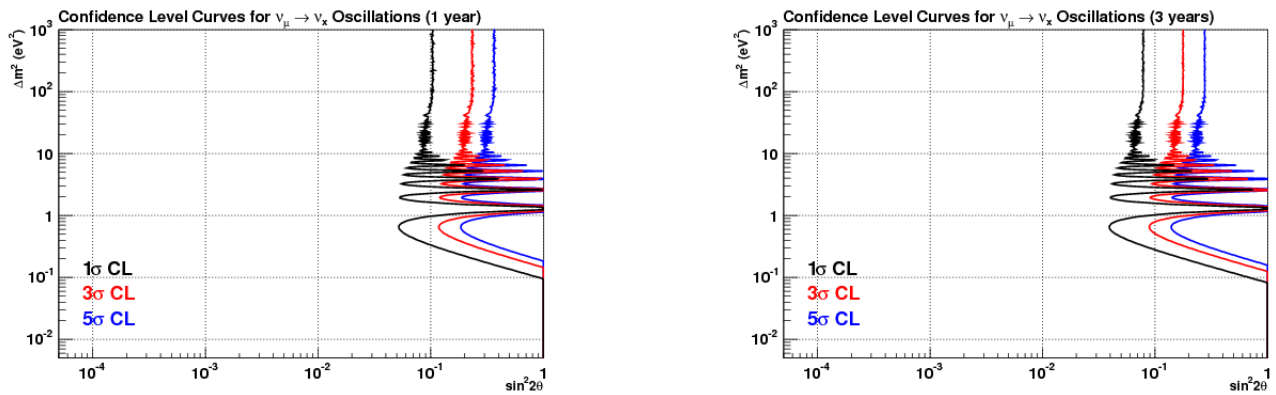


Figure 9.4: OscSNS sensitivity for ν_μ disappearance, for two calendar years of run time (left), and six calendar years of run time (right).

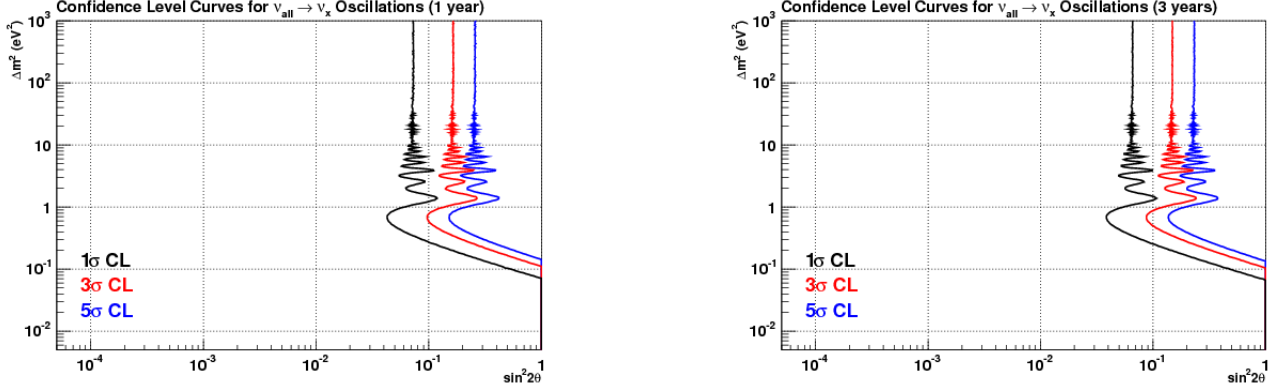


Figure 9.5: OscSNS sensitivity for the total flux disappearance, for two calendar years of run time (left), and six calendar years of run time (right).

9.5.2 ν_e Disappearance Analysis

For the $\nu_e \rightarrow \nu_{sterile}$ search, we look for a deficit in the expected number of charged current $\nu_e \ ^{12}C \rightarrow e^- \ ^{12}N_{gs}$ events. The signature for this reaction is an electron correlated with a positron for $\ ^{12}N_{gs}$ beta decay. The number of events per year is:

$$5.45 \cdot 10^{13} \nu/year/cm^2 \cdot \sigma_{\nu_e \ ^{12}C \rightarrow e^- \ ^{12}N} \cdot 1.94 \cdot 10^{31} \ ^{12}C \text{ targets} \quad (9.7)$$

or 9,410 events per year, where the $\sigma_{\nu_e \ ^{12}C \rightarrow e^- \ ^{12}N_{gs}} = 8.9 \times 10^{-42} \text{ cm}^2$ [23]. Folding in the detector efficiency (50%) and beam-on efficiency (50%), we obtain **2353 ± 123 expected events per year**.

The estimated background for the $\nu_e \ ^{12}C \rightarrow e^- \ ^{12}N_{gs}$ reaction is 1%, which is obtained from the measurement by the LSND experiment [28], as shown in Fig. 9.6.

9.5.3 $\bar{\nu}_\mu \rightarrow \bar{\nu}_e$ Appearance Analysis

The signature for these events is $\bar{\nu}_e$ interactions in the detector, in the form of $\bar{\nu}_e \ ^{12}C \rightarrow e^+ \ ^{11}B \ n$ and $\bar{\nu}_e \ p \rightarrow e^+ \ n$ followed by $np \rightarrow D\gamma(2.2)$ and the emission of a 2.2 MeV γ .

The number of intrinsic (background) $\bar{\nu}_e$ events per year is a sum of the contributions:

$$7.28 \cdot 10^{10} \nu/year/cm^2 \cdot \sigma_{\bar{\nu}_e \ p \rightarrow e^+ \ n} \cdot 3.9 \cdot 10^{31} \text{ free } p \text{ targets}, \quad (9.8)$$

and

$$7.28 \cdot 10^{10} \nu/year/cm^2 \cdot \sigma_{\bar{\nu}_e \ ^{12}C \rightarrow e^+ \ ^{11}B \ n} \cdot 1.94 \cdot 10^{31} \ ^{12}C \text{ targets}, \quad (9.9)$$

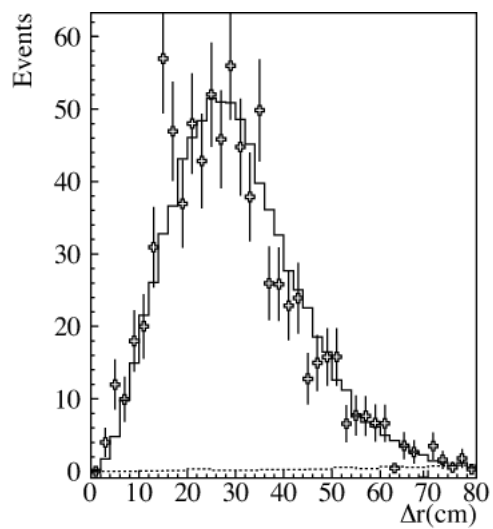


Figure 9.6: The measurement of the reaction $\nu_e \ ^{12}\text{C} \rightarrow e^- \ ^{12}\text{N}_{gs}$ by the LSND experiment. The background, which is estimated to be $\sim 1\%$, is shown as the dotted curve.

or 207 total events per year, where $\sigma_{\bar{\nu}_e p \rightarrow e^+ n} = 0.72 \times 10^{-40} \text{ cm}^2$ and $\sigma_{\bar{\nu}_e {}^{12}\text{C} \rightarrow e^+ {}^{11}\text{B} n} = 2 \times 10^{-42} \text{ cm}^2$ [24]. We expect **42 ± 5 final background events per year**, after reductions due to detector efficiency (50%), beam-on efficiency (50%), and the $E_e > 20 \text{ MeV}$ selection (81%) are applied.

The total number of $\bar{\nu}_\mu$ that can oscillate into $\bar{\nu}_e$ is $5.51 \cdot 10^{13} \nu/\text{year}/\text{cm}^2$. If we assume a 100% transmutation rate, this full amount becomes $\bar{\nu}_e$. The total number of oscillated $\bar{\nu}_e$ events per year is:

$$5.51 \cdot 10^{13} \nu/\text{year}/\text{cm}^2 \cdot \sigma_{\bar{\nu}_e p \rightarrow e^+ n} \cdot 3.9 \cdot 10^{31} \text{ free } p \text{ targets}, \quad (9.10)$$

plus

$$5.51 \cdot 10^{13} \nu/\text{year}/\text{cm}^2 \cdot \sigma_{\bar{\nu}_e {}^{12}\text{C} \rightarrow e^+ {}^{11}\text{B} n} \cdot 1.94 \cdot 10^{31} {}^{12}\text{C} \text{ targets}, \quad (9.11)$$

or 207,350 events per year, where $\sigma_{\bar{\nu}_e p \rightarrow e^+ n} = 0.95 \times 10^{-40} \text{ cm}^2$ and $\sigma_{\bar{\nu}_e {}^{12}\text{C} \rightarrow e^+ {}^{11}\text{B} n} = 3 \times 10^{-42} \text{ cm}^2$ [24].

We expect **120 ± 10 events** after the oscillation probability (0.26%), detector efficiency (50%), beam-on efficiency (50%), and $E_e > 20 \text{ MeV}$ selection (89%) have been applied. The final expected sensitivity for two calendar years and six calendar years run time is shown in Figure 9.7. A detector at 60 meters will give a signal to background of ~ 3 for this search channel.

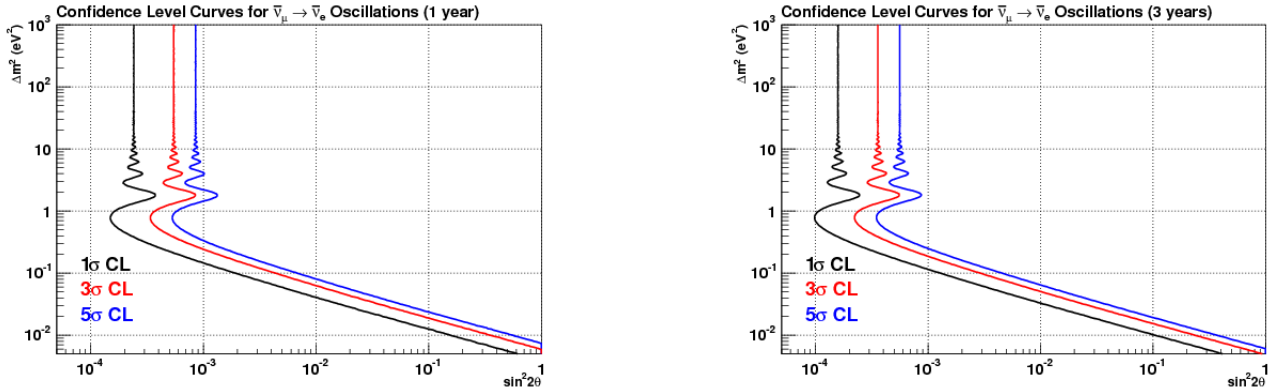


Figure 9.7: OscSNS sensitivity for $\bar{\nu}_\mu \rightarrow \bar{\nu}_e$ oscillations, for two calendar years of run time (left), and six calendar years of run time (right).

9.5.4 $\nu_\mu \rightarrow \nu_e$ Appearance Analysis

The signature of these events are ν_e interactions in the detector, in the form of $\nu_e {}^{12}\text{C} \rightarrow e^- {}^{12}\text{N}_{gs}$, followed by ${}^{12}\text{N}_{gs}$ beta decay. Therefore, there is a 2-fold signature of a 12.5 MeV mono-energetic electron and a correlated positron from beta decay.

The number of intrinsic ν_e background events per year is:

$$5.45 \cdot 10^{13} \nu/\text{year}/\text{cm}^2 \cdot \sigma_{\nu_e {}^{12}\text{C} \rightarrow e^- {}^{12}\text{N}} \cdot 1.94 \cdot 10^{31} {}^{12}\text{C} \text{ targets} \quad (9.12)$$

or 9410 events per year, where the $\sigma_{\nu_e \ 12C \rightarrow e^- \ 12N_{gs}} = 8.9 \times 10^{-42} \text{ cm}^2$ [23]. Folding in the detector efficiency (50%) and beam-on efficiency (50%), we expect 2353 background events per year, spread over the entire event collection window.

However, this calculation does not take into account the timing structure of the beam. The ν_μ come primarily from the π^+ decay, and occur during the beam spill window. Accepting only events occurring in the first 500 ns with respect to the beam on target signal will result in a \sim pure ν_μ beam for use in a $\nu_\mu \rightarrow \nu_e$ oscillation search. Only $\sim 8.6\%$ of all ν_e reaching the detector occur in the first 500 ns. The background expectation is reduced from 2353 to 203 events. An additional cut may be applied to this analysis to further reduce background events. The ν_μ undergoing oscillations come from the π^+ DAR, and are mono-energetic. The energy of the produced electron will appear between 11 and 15 MeV, after smearing due to the energy resolution of the detector. Applying a requirement that the electron be in this energy range reduces the background by a factor of ~ 0.06 . Approximately **12 ± 3 intrinsic background events** are expected per calendar year in this analysis.

The total number of ν_μ s that can oscillate into ν_e is $5.48 \cdot 10^{13} \nu/\text{year}/\text{cm}^2$. If we assume a 100% transmutation rate, this full amount becomes ν_e . The total number of oscillated ν_e events per year is:

$$5.48 \cdot 10^{13} \nu/\text{year}/\text{cm}^2 \cdot \sigma_{\nu_e \ 12C \rightarrow e^- \ 12N} \cdot 1.94 \cdot 10^{31} \ 12C \ \text{targets}, \quad (9.13)$$

or 5316 events per year, where the $\sigma_{\nu_e \ 12C \rightarrow e^- \ 12N_{gs}} = 5 \times 10^{-42} \text{ cm}^2$ [23]. After including factors for detector efficiency (50%), beam-on efficiency (50%), and oscillation probability (0.26%), we expect **3.5 ± 1.5 total oscillated events** per calendar year. Figure 9.8 shows the expected reach for this analysis channel, for two and six calendar years run time.

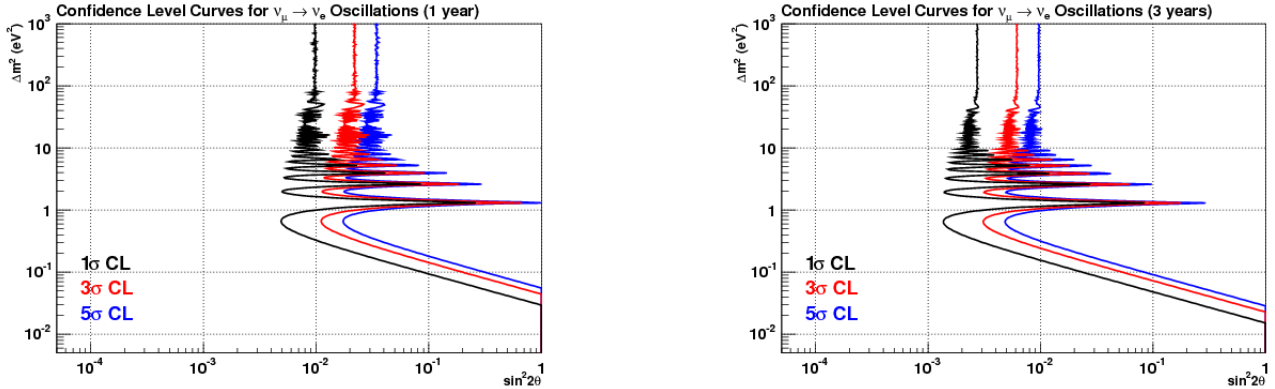


Figure 9.8: OscSNS sensitivity for $\nu_\mu \rightarrow \nu_e$ oscillations, for two calendar years of run time (left), and six calendar years of run time (right).

9.5.5 Oscillation Analysis Summary

Table 9.1 summarizes the expected event sample sizes for the disappearance and appearance oscillation searches, per calendar year. Figures 9.4, 9.5, 9.7, and 9.8 present the expected sensitivity for each of these

analyses. Figures show the expected reach for each analysis for two calendar years and for six calendar years run time.

Channel	Background	Signal
Disappearance Search		
$\nu_\mu \ ^{12}C \rightarrow \nu_\mu \ ^{12}C^*$		
$\nu_e \ ^{12}C \rightarrow \nu_e \ ^{12}C^*$		
$\bar{\nu}_\mu \ ^{12}C \rightarrow \bar{\nu}_\mu \ ^{12}C^*$	1060 ± 36	3535 ± 182
$\nu_\mu \ ^{12}C \rightarrow \nu_\mu \ ^{12}C^*$	224 ± 75	745 ± 42
$\nu_e \ ^{12}C \rightarrow e^- \ ^{12}N_{gs}$	24 ± 13	2353 ± 123
Appearance Search		
$\bar{\nu}_\mu \rightarrow \bar{\nu}_e; \bar{\nu}_e \ ^{12}C \rightarrow e^+ \ ^{11}B \ n$		
$\bar{\nu}_\mu \rightarrow \bar{\nu}_e; \bar{\nu}_e \ p \rightarrow e^+ \ n$	42 ± 5	120 ± 10
$\nu_\mu \rightarrow \nu_e; \nu_e \ ^{12}C \rightarrow e^- \ ^{12}N_{gs}$	12 ± 3	3.5 ± 1.5

Table 9.1: Summary of per calendar year event rate predictions for a detector located at the SNS a distance of 60 meters from the interaction point, at ~ 150 degrees in the backward direction from the proton beam. The first column is oscillation channel, the second column is the expected intrinsic background, and the third column is the expected signal for appearance searches and the total number of events for disappearance searches. All event rates account for a 50% detector efficiency, a 50% beam-on efficiency, and a fiducial volume of 523 m^3 , and are in units of expected events per calendar year. Appearance signal estimates assume a 0.26% oscillation probability.

9.5.6 Cross Section Analyses

The three flagship cross section analyses of OscSNS are the measurement of neutrino-electron elastic scattering $\nu_e e^- \rightarrow \nu_e e^-$, $\nu_\mu C \rightarrow \nu_\mu C^*$ NC scattering, and $\nu_e \ ^{12}C \rightarrow e^- \ ^{12}N_{gs}$ CC scattering.

The number of $\nu_e e^- \rightarrow \nu_e e^-$ events expected per year is:

$$5.45 \cdot 10^{13} \nu/\text{year}/\text{cm}^2 \cdot \sigma_{\nu_e e^- \rightarrow \nu_e e^-} \cdot 8 \cdot 1.94 \cdot 10^{31} e^- \text{ targets}, \quad (9.14)$$

or 2707 events per year, where $\sigma_{\nu_e e^- \rightarrow \nu_e e^-} = 3.2 \times 10^{-43} \text{ cm}^2$ [29].

If we assume 50% detector efficiency and 50% beam-on efficiency, this becomes 677 ± 39 events per calendar year. The best measurement of this interaction so far arises from the LSND experiment in a sample of only 191 events [29], and has a 17% total error. OscSNS will far surpass this measurement in statistics and total uncertainty, with only one year of run time.

The NC $\nu_\mu C$ interaction has been measured by the KARMEN experiment to be $3.2 \pm 0.5 \pm 0.4 \cdot 10^{-42} \text{ cm}^2$ [10]. This measurement was performed using only 86 ν_μ events. While this result is consistent with theory, it has a 20% total error, half of which is due to statistics. OscSNS will collect 745 ± 42 of these events in only one calendar year of run time (Table 9.2), and is expected to have smaller systematic errors. This will allow for the world's most precise cross section measurement; any deviations from theory could indicate the presence of sterile neutrinos.

For the CC $\nu_e {}^{12}\text{C} \rightarrow e^- {}^{12}\text{N}_{gs}$ measurement, we are able to use the entire spectrum of intrinsic ν_e , in contrast to the oscillation search, where we only consider the neutrino flux in the first 500 ns of the beam spill. We expect 2353 ± 123 of these events per calendar year, in the absence of oscillations.

Channel	Event Rate
$\nu_e e^- \rightarrow \nu_e e^-$	677 ± 39
NC $\nu_\mu {}^{12}\text{C} \rightarrow \nu_\mu {}^{12}\text{C}^*$	745 ± 42
CC $\nu_e {}^{12}\text{C} \rightarrow e^- {}^{12}\text{N}_{gs}$	2353 ± 123

Table 9.2: Summary of per calendar year event rate predictions for a detector located at the SNS a distance of 60 meters from the neutrino source, at ~ 150 degrees in the backward direction from the proton beam. The first column is cross section channel, the second column is the expected event rate. All event rates account for a 50% detector efficiency and a 50% beam-on efficiency, and are in units of expected events per year.

Chapter 10

L/E Distributions

Due to the low neutrino energies from π^+ and μ^+ decay at rest, it may be possible to actually observe oscillations in the detector if there is a Δm^2 of approximately 1 eV^2 or greater. Figs. 10.1 and 10.2 show the expected oscillation probability from $\bar{\nu}_e$ appearance as a function of L/E for $\sin^2 2\theta = 0.005$ and $\Delta m^2 = 1 \text{ eV}^2$ and 4 eV^2 , respectively, after 10 calendar years of data collection. This corresponds to 5 years of data collection with continuous beam. The oscillation probability is defined as the event excess divided by the number of events expected for 100% $\bar{\nu}_\mu \rightarrow \bar{\nu}_e$ transmutation, while L is the reconstructed distance traveled by the antineutrino from the mean neutrino production point to the interaction vertex and E is the reconstructed antineutrino energy. The systematic error associated with the L/E distribution is assumed to be negligible; however, the estimated background is approximately 20% of the signal. The L/E resolution is estimated to be approximately 5%. Taking into account the background, an approximate 5σ (10σ) shape distortion is observed for $\Delta m^2 = 1 \text{ eV}^2$ (4 eV^2).

Figs. 10.3 and 10.4 show the expected probability for ν_μ to remain a ν_μ as a function of L/E for $\sin^2 2\theta = 0.15$ and $\Delta m^2 = 1 \text{ eV}^2$ and 4 eV^2 , respectively, after 10 calendar years of data collection. The probability is defined as the number of events observed divided by the number of events expected for no oscillations. L is the reconstructed distance traveled by the neutrino from the mean neutrino production point to the interaction vertex and E is the reconstructed neutrino energy. The L/E resolution is estimated to be approximately 1%. Taking into account the estimated background of 30% that is obtained from the KARMEN experiment after subtracting the fast neutron background [10], an approximate 2σ (3σ) shape distortion is observed for $\Delta m^2 = 1 \text{ eV}^2$ (4 eV^2).

Figs. 10.5 and 10.6 show the expected probability for ν_e to remain a ν_e as a function of L/E for $\sin^2 2\theta = 0.15$ and $\Delta m^2 = 1 \text{ eV}^2$ and 4 eV^2 , respectively, after 10 calendar years of data collection. The probability is defined as the number of events observed divided by the number of events expected for no oscillations. L is the reconstructed distance traveled by the neutrino from the mean neutrino production point to the interaction vertex and E is the reconstructed neutrino energy. The L/E resolution is estimated to be approximately 5%. Taking into account the estimated background of 1% that was obtained in LSND [28], an approximate 3σ (5σ) shape distortion is observed for $\Delta m^2 = 1 \text{ eV}^2$ (4 eV^2).

Table 10.1 shows the average shape-only χ^2 values (for 10 data bins assuming no oscillations) after 10

calendar years of data taking for $\bar{\nu}_e$ appearance, ν_e disappearance, and ν_μ disappearance, taking into account the expected backgrounds. Also shown are the corresponding probabilities for no oscillations. Two sets of oscillation parameters are assumed for each case: $(\Delta m^2, \sin^2 2\theta) = (0.91eV^2, 0.0053)$ and $(3.6eV^2, 0.0053)$ for $\bar{\nu}_e$ appearance, and $(\Delta m^2, \sin^2 2\theta) = (0.91eV^2, 0.169)$ and $(3.6eV^2, 0.169)$ for ν_e and ν_μ disappearance. Significant evidence for neutrino oscillations can be obtained by performing a simple shape-only fit to the L/E distributions.

If the absolute neutrino flux normalization can be obtained by fitting the data, then the significance of the fits to the χ^2 distributions improves greatly. Table 10.2 shows the average normalized χ^2 values (for 10 data bins assuming no oscillations) after 10 calendar years of data taking for $\bar{\nu}_e$ appearance, ν_e disappearance, and ν_μ disappearance, taking into account the expected backgrounds. Also shown are the corresponding probabilities for no oscillations. Very significant evidence for neutrino oscillations can be obtained by performing a normalized fit to the L/E distributions.

Oscillation	Δm^2	$\sin^2 2\theta$	χ^2	No Oscillation Probability	Significance
$\bar{\nu}_e$ Appearance	0.91 eV ²	0.0053	123.3	$< 10^{-10}$	$> 6\sigma$
$\bar{\nu}_e$ Appearance	3.6 eV ²	0.0053	166.3	$< 10^{-10}$	$> 6\sigma$
ν_e Disappearance	0.91 eV ²	0.169	25.4	0.0046	2.8σ
ν_e Disappearance	3.6 eV ²	0.169	49.8	2.9×10^{-7}	5σ
ν_μ Disappearance	0.91 eV ²	0.169	15.7	0.1085	1.6σ
ν_μ Disappearance	3.6 eV ²	0.169	25.1	0.0051	2.7σ

Table 10.1: The average shape-only χ^2 values (for 10 data bins assuming no oscillations) after 10 calendar years of data taking for $\bar{\nu}_e$ appearance, ν_e disappearance, and ν_μ disappearance, taking into account the expected backgrounds. Also shown are the corresponding probabilities for no oscillations.

Oscillation	Δm^2	$\sin^2 2\theta$	χ^2	No Oscillation Probability	Significance
$\bar{\nu}_e$ Appearance	0.91 eV ²	0.0053	11,930	$< 10^{-10}$	$> 6\sigma$
$\bar{\nu}_e$ Appearance	3.6 eV ²	0.0053	2992	$< 10^{-10}$	$> 6\sigma$
ν_e Disappearance	0.91 eV ²	0.169	468.2	$< 10^{-10}$	$> 6\sigma$
ν_e Disappearance	3.6 eV ²	0.169	126.1	$< 10^{-10}$	$> 6\sigma$
ν_μ Disappearance	0.91 eV ²	0.169	33.7	0.0002	3.6σ
ν_μ Disappearance	3.6 eV ²	0.169	25.9	0.0038	2.9σ

Table 10.2: The average normalized χ^2 values (for 10 data bins assuming no oscillations) after 10 calendar years of data taking for $\bar{\nu}_e$ appearance, ν_e disappearance, and ν_μ disappearance, taking into account the expected backgrounds. Also shown are the corresponding probabilities for no oscillations.

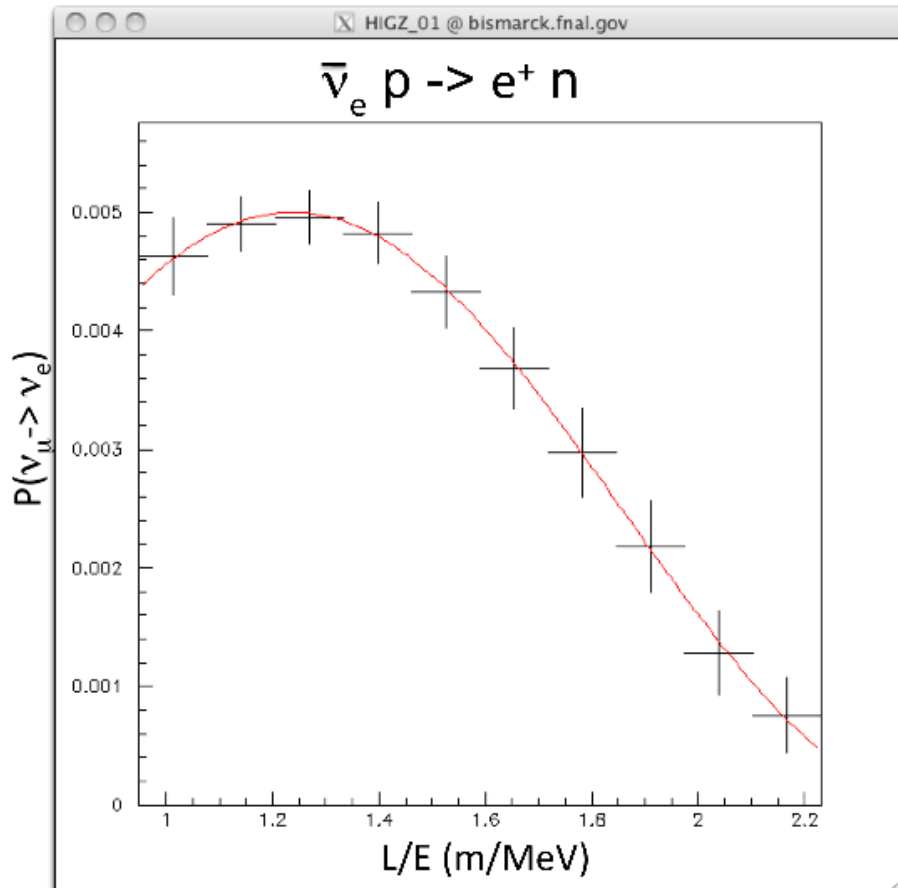


Figure 10.1: The expected oscillation probability from $\bar{\nu}_e$ appearance as a function of L/E for $\sin^2 2\theta = 0.005$ and $\Delta m^2 = 1 \text{ eV}^2$, for ten *calendar* years of data collection at 50% beam live-time.

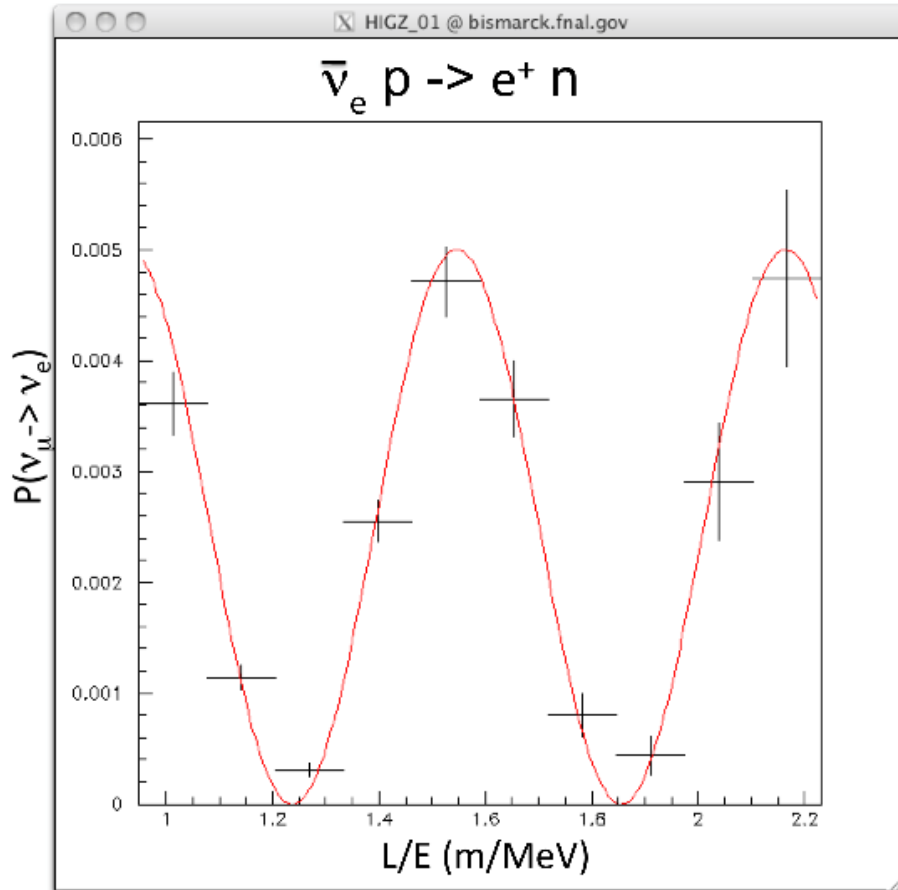


Figure 10.2: The expected oscillation probability from $\bar{\nu}_e$ appearance as a function of L/E for $\sin^2 2\theta = 0.005$ and $\Delta m^2 = 4 \text{ eV}^2$, for ten *calendar* years of data collection at 50% beam live-time.

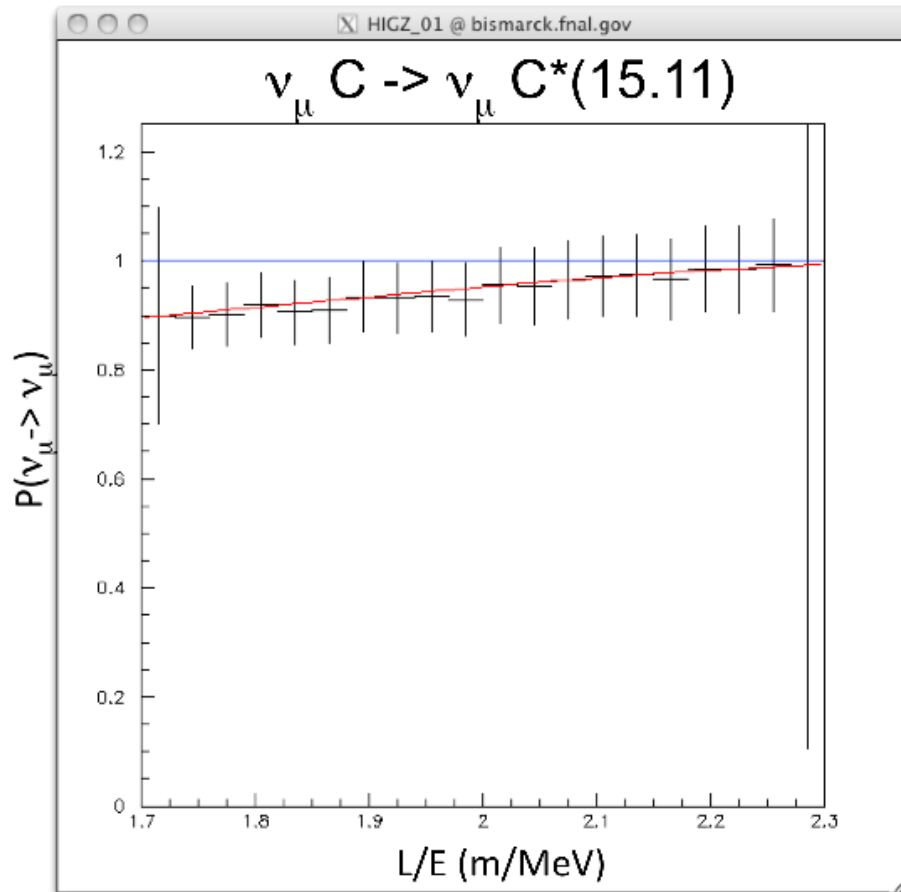


Figure 10.3: The expected probability for ν_{μ} to remain a ν_{μ} as a function of L/E for $\sin^2 2\theta = 0.15$ and $\Delta m^2 = 1 \text{ eV}^2$, for ten *calendar* years of data collection at 50% beam live-time.

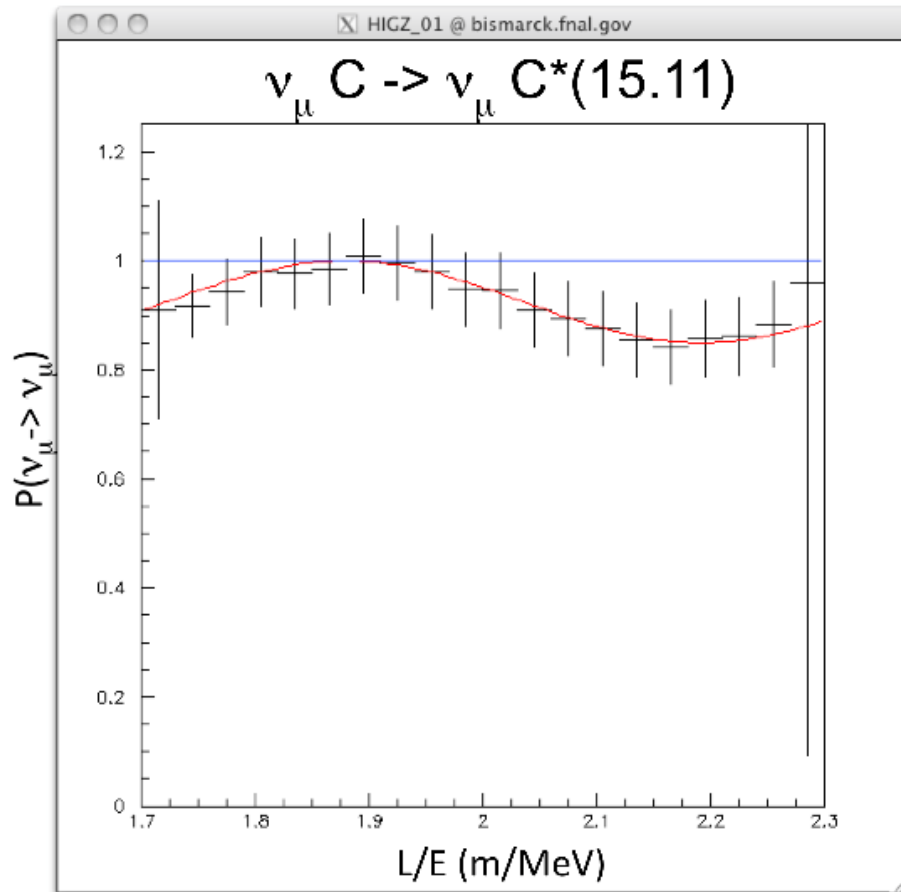


Figure 10.4: The expected probability for ν_{μ} to remain a ν_{μ} as a function of L/E for $\sin^2 2\theta = 0.15$ and $\Delta m^2 = 4 \text{ eV}^2$, for ten *calendar* years of data collection at 50% beam live-time.

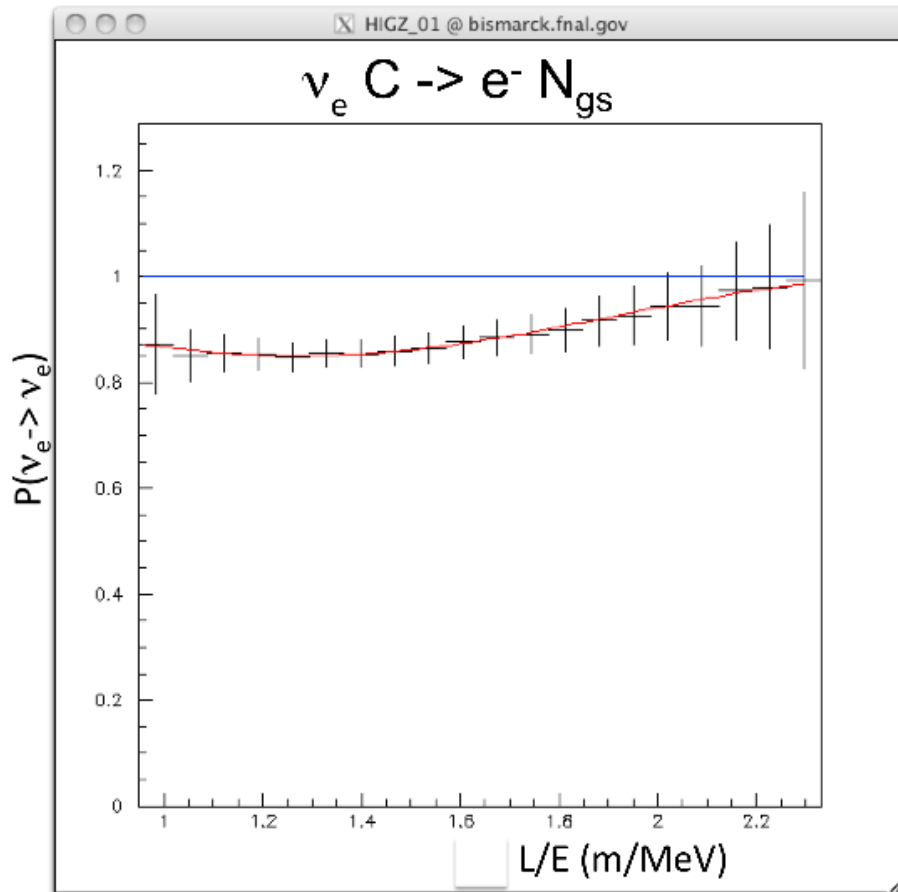


Figure 10.5: The expected probability for ν_e to remain a ν_e as a function of L/E for $\sin^2 2\theta = 0.15$ and $\Delta m^2 = 1 \text{ eV}^2$, for ten *calendar* years of data collection at 50% beam live-time.

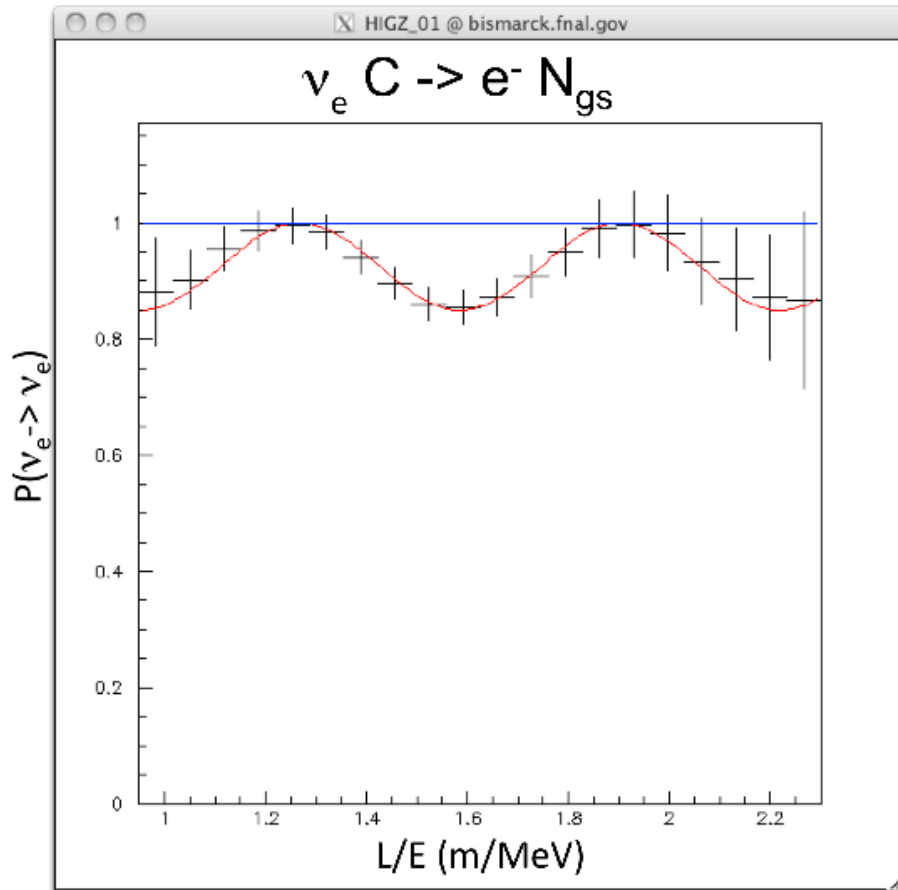


Figure 10.6: The expected probability for ν_e to remain a ν_e as a function of L/E for $\sin^2 2\theta = 0.15$ and $\Delta m^2 = 4 \text{ eV}^2$, for ten *calendar* years of data collection at 50% beam live-time.

Chapter 11

Cost & Schedule

Table 11.1 shows a breakdown of the OscSNS cost estimate, which is based on the MiniBooNE construction costs. The largest component is the civil construction cost of \$5.461M, which has been estimated by the BWSC company of Knoxville, TN. The total estimated cost of the OscSNS experiment is \$21.852M, including contingency ($\sim 54\%$) and escalation ($\sim 5\%$). The OscSNS construction is assumed to start in the beginning of FY15 and last for 3 years. Expenditures per year are estimated to be \$5896K, \$9048K, and \$6908K in FY15, FY16, and FY17, respectively.

Item	Cost (\$K)	Contingency	Escalation	Total Cost (\$K)
Phototubes	5219	30%	4%	7056
Preamps	53	20%	12%	71
Electronics	665	30%	12%	969
DAQ	50	20%	12%	67
Civil Constr.	5462	100%	0%	10,924
Plumbing	20	20%	8%	26
Oil	1034	20%	2%	1265
Detector Tank	1030	30%	8%	1446
Support	20	30%	8%	28
Total	13,553	54%	5%	21,852

Table 11.1: A breakdown of the OscSNS cost estimate, including contingency and escalation. The OscSNS construction is assumed to start in the beginning of FY15 and last for 3 years.

The OscSNS cost estimate can be reduced by reusing the MiniBooNE oil and PMTs. The use of additional parts from MiniBooNE may also be considered.

Chapter 12

The OscSNS Near Detector

12.0.7 The OscSNS Near Detector

We would ideally like to install two neutrino detectors at the SNS. A near detector for OscSNS will provide a cross check for the neutrino flux normalization. A space adjacent to BL-18 has been identified as a possible location for such a detector in terms of proximity to the neutrino source, available space, and maximum floor loading. Given the current constraints, the detector would have a footprint of $3.7 \times 5.1 \times 3.4$ m. The outer 40 cm consists of passive shielding, followed by a 25-cm-thick active veto, which is optically isolated from the inner volume of the detector. The active veto is painted white to enhance reflections, and is instrumented with about 120 5-inch PMTs. The inner detector is instrumented with 808 5-inch PMTs, which correspond to the same photocathode surface coverage as the main detector, namely 25%. These PMTs are embedded within the active veto, and are mounted such that their equator is flush with the optical barrier. Additional flat photodetection devices, currently under development at the Argonne National Laboratory, could also be interspersed with the standard 5-inch PMTs, assuming that these devices are fully operational by construction time.

The inner detector is painted black (to avoid reflections) and is filled with exactly the same active medium as the main detector. Assuming a neutrino production rate of 2.8×10^{22} per year at 100% SNS efficiency, the neutrino flux at the location of the near detector yields $\Phi = 5.57 \times 10^{14} \text{ cm}^{-2} \text{ yr}^{-1}$, which in turn will yield an event rate of 183.4 per year per cubic meter of fiducial volume for the $\nu_e C \rightarrow e^- {}^{12}\text{N}_{gs}$ reaction. This reaction is well-known theoretically, while its two-fold signature (i.e., the space-time correlation between the electron and the positron from the subsequent ${}^{12}\text{N}_{gs}$ β -decay) gives a strong discrimination from backgrounds (in particular the relatively abundant beam-related neutrons given the proximity of the neutron beam lines).

Assuming a fiducial volume of 7.4 m^3 , which corresponds to a minimum distance of 30 cm from the edge of the optical barrier, the near detector could record a total of 1620 $\nu_e C \rightarrow e^- {}^{12}\text{N}_{gs}$ events (assuming a combined efficiency of 40% for the SNS beam and the near detector), corresponding to a 2.5% statistical error.

Chapter 13

Appendix A - Letters of Support

This space is reserved for letters of support.

Chapter 14

Appendix B - BWSC Cost Estimate

This space is reserved for a complete civil engineering study, performed by Barge Waggoner Sumner and Cannon, Inc., of Knoxville, TN. The survey is in the final stages, and will be completed and appended shortly.

Bibliography

- [1] G. L. Fogli, E. Lisi, A. Marrone, D. Montanino, A. Palazzo, and A. M. Rotunno, arXiv:1205.5254 (2012).
- [2] C. Athanassopoulos *et al.*, Phys. Rev. Lett. 75, 2650 (1995); 77, 3082 (1996); 81, 1774 (1998); Phys. Rev. C. **58**, 2489 (1998); A. Aguilar *et al.*, Phys. Rev. D 64, 112007 (2001).
- [3] A. A. Aguilar-Arevalo *et al.*, Phys. Rev. Lett. 105, 181801 (2010); Phys. Rev. Lett. 110, 161801 (2013).
- [4] C. Giunti and M. Laveder, Phys. Rev. C 83, 065504 (2011).
- [5] G. Mention, M. Fechner, T. Lasserre, T. A. Mueller, D. Lhuillier, M. Cribier, and A. Letourneau, Phys. Rev. D 83, 073006 (2011).
- [6] J. M. Conrad, C. M. Ignarra, G. Karagiorgi, M. H. Shaevitz, and J. Spitz, arXiv:1207.4765 [hep-ex] (2012).
- [7] Joachim Kopp, Pedro A. N. Machado, Michele Maltoni, and Thomas Schwetz, arXiv:1303.3011 [hep-ph] (2013).
- [8] The Spallation Neutron Source (SNS) is an accelerator-based source built in Oak Ridge, Tennessee, by the U.S. DOE, <http://sns.gov/>. Also see <http://www.phy.ornl.gov/workshops/sns2/> for details on the neutrino source and cross section detector ν -SNS.
- [9] A. A. Aguilar-Arevalo *et al.*, Phys. Rev. Lett. 102, 101802 (2009).
- [10] B. Armbruster *et al.*, Phys. Rev. D 65, 112001 (2002).
- [11] D. Adey *et al.*, arXiv:1305.1419 [physics.acc-ph].
- [12] C. Athanassopoulos *et al.*, Nuclear Instruments and Methods in Physics Research A **388**, 149 (1997).
- [13] B. A. Moffat, *et al.*, Nuclear Instruments and Methods in Physics Research A **554**, 255 (2005) [nucl-ex/0507026].
- [14] S. Agostinelli, *et al.*, Nuclear Instruments and Methods in Physics Research A **506**, 250 (2003); <http://geant4.cern.ch>.
- [15] <http://reat.space.qinetiq.com/gps/>.

- [16] K. A. Walaron, UKNF Note 30: Simulations of Pion Production in a Tantalum Rod Target using GEANT4 with comparison to MARS; http://hepunix.rl.ac.uk/uknf/wp3/uknfnote_30.pdf.
- [17] T. Suzuki, D. F. Measday, J. P. Roaisvig, Phys. Rev. C, **35**, 2212 (1987).
- [18] R. Brun, F. Rademakers, Nuclear Instruments and Methods in Physics Research A **389**, 81 (1997); <http://root.cern.ch>.
- [19] http://www.physics.uc.edu/~johnson/Boone/oil_page/Index.html.
- [20] R. A. Reeder *et al.*, Nuclear Instruments and Methods in Physics Research A **334**, 353 (1993).
- [21] J. B. Birks, Theory and Practice of Scintillation Counting (Pergamon. Oxford, 1964).
- [22] M. Fukugita, Y. Kohyama, K. Kubodera, Phys. Lett. B **212**, 139 (1988).
- [23] E. Kolbe, K. Langanke, and P. Vogel, Nucl. Phys. A **652**, 91 (1999).
- [24] P. Vogel and J. F. Beacom. Phys. Rev. D **60**, 053003 (1999).
- [25] M. Sorel, J. M. Conrad and M. Shaevitz, Phys. Rev. D **70**, 073004 (2004).
- [26] G. Karagiorgi, Z. Djurcic, J. M. Conrad, M. H. Shaevitz and M. Sorel, Phys. Rev. D **80**, 073001 (2009) [Erratum- *ibid.* D **81**, 039902 (2010)].
- [27] C. Giunti and M. Laveder, Phys. Lett. B **706**, 200 (2011). C. Giunti and M. Laveder, Phys. Rev. D **84**, 073008, (2011).
- [28] L. B. Auerbach *et al.*, Phys. Rev. D **64**, 065501 (2001).
- [29] L. B. Auerbach *et al.*, Phys. Rev. D **63**, 112001 (2001).